European Polymer Journal 243 (2026) 114464

Contents lists available at ScienceDirect

European Polymer Journal

journal homepage: www.elsevier.com/locate/europolj

How chain stereoconfiguration and molecular weight influence Poly(propylene oxide) crystallization

Juan Torres-Rodríguez [a], Charlotte Fornaciari [b,c], Ricardo A. Pérez-Camargo [a,**], Agurtzane Mugica [a], Manuela Zubitur [d], Giovanni Preda [b], Dario Pasini [b], Olivier Coulembier [c,**], Alejandro J. Müller [a,e,*]

[a] POLYMAT and Department of Polymers and Advanced Materials: Physics, Chemistry and Technology, Faculty of Chemistry, University of the Basque Country UPV/EHU, Paseo Manuel de Lardizabal, 3, 20018 Donostia-San Sebastián, Spain
[b] Department of Chemistry and INSTM Unit, University of Pavia, Viale Taramelli, 12, 27100 Pavia, Italy
[c] Laboratory of Polymeric and Composite Materials, University of Mons, Place du Parc 23, 7000 Mons, Belgium
[d] Faculty of Engineering of Gipuzkoa, University of the Basque Country UPV/EHU, Plaza de Europa, 1, 20018 Donostia-San Sebastián, Spain
[e] IKERBASQUE, Basque Foundation for Science, Plaza Euskadi 5, Bilbao 48009, Spain

ARTICLE INFO

Keywords:
Poly(propylene oxide)
Crystallization
Molecular weight
Stereoconfiguration
Racemic blends

ABSTRACT

We report on the synthesis and crystallization behavior of poly(propylene oxide) (PPO) with tunable molar masses and defined stereoconfiguration (PPO-*R* and PPO-*S*), obtained through controlled oxyanionic ring-opening polymerization using hexaethylene glycol (EG6) as the initiator, with an equimolar mixture of potassium acetate (KOAc) and 18-crown-6 ether (18C6). This method provides access to well-defined enantiopure PPO samples across a broad range of number-average molecular weights (M_n), allowing for the independent evaluation of how molecular weight and stereoconfiguration influence crystallization. Morphology, thermal transitions, structural features, and crystallization kinetics were analyzed using Polarized Light Optical Microscopy (PLOM), Differential Scanning Calorimetry (DSC), in situ Wide- and Small-angle X-ray Scattering (WAXS/SAXS), and, for the first time in PPO, thermal fractionation via Successive Self-nucleation and Annealing (SSA). Both PPO-*R* and PPO-*S* display increasing thermal transitions with M_n, eventually reaching a plateau. Although they crystallize into identical orthorhombic unit cells, the two enantiomers show small yet consistent and reproducible kinetic differences across all techniques used: PPO-*R* crystallizes faster at low M_n, while PPO-*S* does so at high M_n. This crossover, related to a specific M_n value, though unexpected for two enantiomeric polymers forming identical lattices, was consistently observed by different experimental techniques across nucleation, spherulitic growth, overall crystallization rate, and SSA fractionation. This confirms the effect is real and experimentally reliable. We provide a mechanistic interpretation suggesting that stereoconfiguration could be influencing melt dynamics, likely through subtle differences in chain diffusion and entanglement onset. Racemic PPO-*R*:*S* blends were prepared at both low and high M_n. No stereocomplexation was observed; however, these blends exhibited lower melting transitions and slower crystallization kinetics than the enantiopure samples, possibly due to packing frustration between chains of opposite helicities. Overall, molecular weight and stereoconfiguration are effective parameters for tuning PPO crystallization kinetics, thereby enabling PPO-based blends and copolymers with controlled crystallization rates and expanded processability in biodegradable polymer systems.

* Corresponding author at: POLYMAT and Department of Polymers and Advanced Materials: Physics, Chemistry and Technology, Faculty of Chemistry, University of the Basque Country UPV/EHU, Paseo Manuel de Lardizabal, 3, 20018 Donostia-San Sebastián, Spain.
** Corresponding authors.
E-mail addresses: ricardoarpad.perez@ehu.eus (R.A. Pérez-Camargo), olivier.coulembier@umons.ac.be (O. Coulembier), alejandrojesus.muller@ehu.es (A.J. Müller).

https://doi.org/10.1016/j.eurpolymj.2025.114464
Received 10 October 2025; Received in revised form 15 December 2025; Accepted 19 December 2025
Available online 24 December 2025

1. Introduction

Extensive research is underway to develop biobased and biodegradable polymers with an intrinsically low environmental impact.[1,2] Blending and copolymerization are common methods for enhancing the properties of biobased and biodegradable polymers. Polyethers can introduce additional degradation sites through their ether linkages when blended or copolymerized with poly(lactic acid) (PLA), which primarily degrades in its amorphous regions through ester scission. [3–8] These hybrid systems offer opportunities to accelerate degradation while improving processability and the tunability of mechanical and thermal properties. [9] Among polyethers, poly(ethylene oxide) (PEO) has been the most widely explored. It is widely used in block copolymers and PLA blends, [9–14] yet PEO/PLA blends often undergo phase separation during crystallization, a limitation that compromises transparency and affects water uptake and solubility. [15–17] These drawbacks motivate the search for alternative polyethers that can enhance miscibility and performance in biodegradable polyester formulations.

Poly(propylene oxide) (PPO) has emerged as a promising yet underexplored candidate. PPO is a chiral polyether (Scheme 1) derived from the ring-opening polymerization of propylene oxide, in which each repeating unit contains a stereogenic center at the tertiary carbon. Depending on the polymerization catalyst, isotactic PPO-*R* and PPO-*S*, syndiotactic, or atactic variants can be obtained, each displaying distinct physical properties.[18] Commercial PPO is typically atactic and amorphous, whereas isotactic PPOs (*i*PPO) are semicrystalline, exhibiting a melting temperature (T_m) around 67 °C and a low glass transition temperature (T_g ~ −76 °C). [19–21] Its refractive index (1.45–1.46) [22], closely matches that of PLA (1.45–1.50) [23], ensuring transparency in blends. PPO is also biocompatible and non-toxic,[19,20] and its hydroxy-telechelic derivatives are widely used as polyether polyols in polyurethane foams, elastomers, and adhesives, [24,25] highlighting its industrial maturity and availability.

Despite these advantages, the crystallization behavior of *i*PPO remains poorly understood. Early work by Magill et al., [22] Booth et al., [26] and Cooper et al., [27] described crystalline forms and optical textures of *i*PPO but did not clearly differentiate between the *R* and *S* enantiomers, nor did they explore the influence of molecular weight. Later studies [28,29] focused mainly on melt-crystallized morphology (e.g., banded spherulites and lamellar organization) and on radial growth rates under specific nucleating conditions, but a systematic decoupling of the influence of stereoconfiguration and number-average molecular weight (M_n) on overall crystallization has never been reported. Likewise, no study to date has examined the crystallization behavior of racemic PPO-*R*:*S* mixtures, and the possibility of stereocomplex or racemate formation remains unexplored.

A broader look at chiral polymer crystallization highlights why such a study is needed. The benchmark system PLLA/PDLA illustrates how molecular handedness can dramatically affect crystallization: Both poly (L-lactic acid) (PLLA) and poly(D-lactic acid) (PDLA) can be synthesized with high optical purity and, under comparable M_n and thermal histories, each enantiomer homocrystallizes into the same α-form with essentially identical melting/crystallization behavior, consistent with their thermodynamic equivalence as enantiomeric polymers.[30–32] However, PDLA is often described as amorphous in the literature because commercial samples typically have a lower molecular weight or slightly lower optical purity, which strongly retards homocrystallization. While the effect of molecular weight on the crystallization of PLLA has been systematically investigated, [33,34] no analogous series exists for PDLA. Most studies employ a single PDLA grade, typically of lower M_n, as a reference or for stereocomplex formation, precluding any rigorous comparison of molecular-weight dependence between the two enantiomers. The influence of M_n has therefore been examined almost exclusively at values well above the entanglement molecular weight (M_e ~ 8–10 kg/mol), [35] where chain reptation dominates melt dynamics and effectively masks any subtle influence of stereoconfiguration on nucleation or growth kinetics. Consequently, potential kinetic asymmetries between PLLA and PDLA remain experimentally unexplored in the case of homocrystallization. The effects of molecular weight have been studied in the case of stereocomplexation. [36]

In contrast, for poly(3-hydroxybutyrate) (PHB), comparisons between enantiomers are experimentally limited: only PHB-*R* is naturally produced by bacterial synthesis, [37] whereas PHB-*S* can be obtained only through challenging stereoselective polymerization of *(S)*-β-butyrolactone, yielding low-molar-mass oligomers. [38] Consequently, no direct comparison between high-M_n PHB-*R* and PHB-*S* has been reported, leaving the potential influence of molecular chirality largely unexplored in this system.

When mixtures of opposite enantiomers are possible, markedly different behaviors arise. In PLLA/PDLA blends, chains of opposite chirality co-crystallize into highly stable stereocomplex crystals (T_m ~ 230 °C) that show slower nucleation but enhanced thermal and mechanical stability. [39–41] This occurs particularly with PLLA and PDLA of low M_n and equal molar ratio.[39] By contrast, PHB-*R*:*S* mixtures do not form stereocomplexes; the presence of the opposite enantiomer disrupts regular chain packing, markedly depressing T_m and crystallization temperature (T_c) and yielding materials with very low crystallinity or even a partially amorphous morphology. [42] These two cases illustrate the extremes of chiral crystallization behavior, cooperative stabilization versus packing frustration, and demonstrate how chirality can profoundly influence crystallization when accessible.

Advances in isospecific oxyanionic ring-opening polymerization over the last decade have finally enabled the synthesis of PPO-*R* and PPO-*S* with controllable molecular weight and narrow dispersity [24] opening the possibility of rigorously evaluating how M_n and stereoconfiguration jointly affect crystallization in a chiral polyether. This is particularly compelling because, in principle, enantiomeric polymers such as PPO-*R* and PPO-*S* should be thermodynamically equivalent in an achiral environment. Nevertheless, subtle kinetic or morphological differences could arise from their opposite helical sense, especially in systems with low entanglement molecular weight, high chain flexibility, and fast

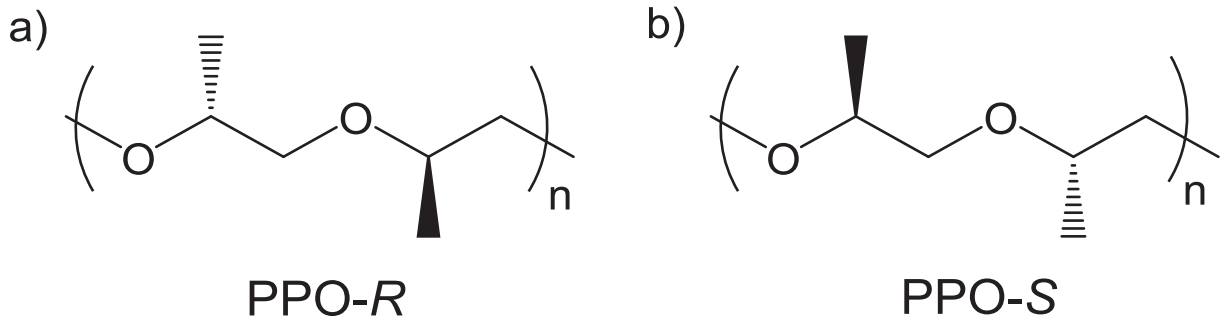

Scheme 1. General structure of a) PPO-*R* and b) PPO-*S*.

segmental dynamics.

In this study, we present the first detailed and controlled investigation of PPO-*R*, PPO-*S*, and PPO-*R*:*S* blends across a wide M_n range, using Differential Scanning Calorimetry (DSC), Wide- and Small-angle X-ray scattering (WAXS/SAXS), Polarized-light Optical Microscopy (PLOM), and Successive Self-nucleation and Annealing (SSA). We clarify the separate effects of molecular weight and stereoconfiguration on thermal transitions, crystallization kinetics, lamellar structure, and spherulitic morphology. This comprehensive analysis offers new insights into how molecular chirality influences crystallization and melt behavior in PPO, and it provides rational design principles for adjusting crystallization properties and compatibility in PPO-based biodegradable blends, especially in PLA/PPO formulations, where controlling crystallization is crucial for transparency, processability, and performance.

2. Experimental

2.1. Materials

(±)-Propylene oxide ((*R, S*)-PO, ≥ 99 %, Aldrich), (*R*)-(+)-propylene oxide, and (*S*)-(−)-propylene oxide ((*R*) and (*S*)-PO, ≥ 99 %, Aldrich) were dried over CaH_2, distilled and stored over molecular sieves. Hexaethylene glycol (EG6, Merck, $M_n \sim 300$ g mol^{-1}) was dried by three azeotropic distillations using tetrahydrofuran (THF), while potassium acetate (KOAc, ≥ 99 %, VWR) was dried by heating at 100 °C under vacuum for 48 h, and 18-Crown ether-6 (18C6, 99 %, ACROS Organics) was dried by three azeotropic distillations of THF. All monomers, catalyst components, and solvents were stored in a glovebox under controlled O_2 and H_2O levels ($O_2 \leq 6$ ppm, $H_2O \leq 1$ ppm). THF was purified using an MBraun SPS system. All reagents were used as received unless otherwise specified.

2.2. Synthesis procedure

2.2.1. General procedure for (±)-PO homopolymerization

In a glove box, a vial, equipped with a stir bar, was charged with EG6 (20.6 mg, 0.068 mmol), KOAc (6.7 mg, 0.068 mmol), 18C6 (18.2 mg, 0.068 mmol), and (±)-PO (0.717 g, 12.3 mmol). The reaction was carried out at 21 °C, yielding *rac*-PPO as a clear viscous oil. The product was analyzed by ^{1}H and ^{13}C NMR spectroscopy. The number-average molar mass (M_n) and the dispersity ($Đ_M = M_w/M_n$) were determined by SEC analysis.

^{1}H NMR ($CDCl_3$, 500 MHz): δ 1.08 − 1.12 (m, −C$\underline{H}_3$), 3.36 − 3.58 (broad m, −O − C$\underline{H}_2$ − C$\underline{H}$(CH$_3$) − O −), 3.64 (broad m, −O − C$\underline{H}_2$ − C$\underline{H}_2$ − O −), 3.91 − 3.95 (m, − C$\underline{H}$(CH$_3$) − OH). ^{13}C NMR ($CDCl_3$, 101 MHz): δ 17.45 (−$\underline{C}$H$_3$), 73.09 (−O − $\underline{C}$H$_2$ − CH(CH$_3$) − O−, rrm or mrr), 73.42 (−O − $\underline{C}$H$_2$ − CH(CH$_3$) − O−, m), 75.23 (−O − CH$_2$ − $\underline{C}$H(CH$_3$) − O−, rr), 75.47 (−O − CH$_2$ − $\underline{C}$H(CH$_3$) − O−, mr + rm), 75.66 (−O − CH$_2$ − $\underline{C}$H(CH$_3$) − O−, mm).

2.2.2. General procedure for (R)-PO homopolymerization

In a glove box, a vial equipped with a stir bar was charged with EG6 (15.5 mg, 0.051 mmol), KOAc (5.1 mg, 0.051 mmol), 18C6 (13.6 mg, 0.051 mmol), and (*R*)-PO (2.19 g, 37.7 mmol). The reaction was carried out at 21 °C. Kinetic monitoring was performed by SEC and ^{1}H NMR spectroscopy. Upon completion, the polymer was isolated by precipitation from a THF/*n*-heptane (2:7), yielding a white powder (1.90 g).

^{1}H NMR ($CDCl_3$, 500 MHz): δ 1.11 − 1.16 (m, −C$\underline{H}_3$), 3.40 − 3.56 (broad m, −O − C$\underline{H}_2$ − C$\underline{H}$(CH$_3$) − O −), 3.64 (broad m, −O − C$\underline{H}_2$ − C$\underline{H}_2$ − O −), 3.92 − 3.95 (m, − C$\underline{H}$(CH$_3$) − OH). ^{13}C NMR ($CDCl_3$, 101 MHz): δ 17.49 (−$\underline{C}$H$_3$), 73.56 (−O − $\underline{C}$H$_2$ − CH(CH$_3$) − O−, m), 75.70 (−O − CH$_2$ − $\underline{C}$H(CH$_3$) − O−, mm).

2.2.3. General procedure for (S)-PO homopolymerization

In a glove box, a vial equipped with a stir bar was charged with EG6 (7.3 mg, 0.024 mmol), KOAc (2.38 mg, 0.024 mmol), 18C6 (6.6 mg, 0.024 mmol), and (*S*)-PO (1.03 g, 17.7 mmol). The reaction was carried out at 21 °C. Kinetic monitoring was performed by SEC and ^{1}H NMR spectroscopy. Upon completion, the polymer was isolated by precipitation from a THF/n-heptane (2:7) mixture, yielding a white powder (95 mg).

^{1}H NMR ($CDCl_3$, 500 MHz): δ 1.11 − 1.16 (m, −C$\underline{H}_3$), 3.40 − 3.56 (broad m, −O − C$\underline{H}_2$ − C$\underline{H}$(CH$_3$) − O −), 3.64 (broad m, −O − C$\underline{H}_2$ − C$\underline{H}_2$ − O −), 3.92 − 3.95 (m, − C$\underline{H}$(CH$_3$) − OH). ^{13}C NMR ($CDCl_3$, 101 MHz): δ 17.58 (−$\underline{C}$H$_3$), 73.58 (−O − $\underline{C}$H$_2$ − CH(CH$_3$) − O−, m), 75.71 (−O − CH$_2$ − $\underline{C}$H(CH$_3$) − O−, mm).

2.2.4. General procedure for preparing PPO-R/PPO-S (PPO-R:S) racemic blend

Two sets of enantiomeric PPO samples (*R* and *S*) with comparable $M_{n,NMR}$ (~ 2,700 and ~ 11,400 g/mol) were combined in a 1:1 wt ratio and dissolved in chloroform. The resulting solution was added dropwise to cold methanol (ten times volume excess), inducing precipitation. The solid was collected by filtration and dried under vacuum at room temperature prior to the analysis.

2.3. Characterization methods

2.3.1. Nuclear magnetic resonance (NMR) spectroscopy

^{1}H and ^{13}C NMR spectra were recorded at room temperature using a Bruker AVANCEII 500 MHz spectrometer. Chemical shifts were used to confirm polymer structure, tacticity, and end groups. Detailed acquisition parameters are provided in the Supporting Information (Section S1).

2.3.2. Size exclusion chromatography (SEC)

SEC analyses were performed in THF at 35 °C using a Triple Detection Polymer Laboratories liquid chromatograph equipped with a refractive index, UV, light, and capillary-viscometer detectors. Number-average molar mass (M_n) and dispersity ($Đ_M$) were determined using universal calibration and monitored throughout polymerization. Instrumental configuration and column specifications are given in the SI (Section S1).

2.3.3. Circular dichroism (CD) spectroscopy

CD spectra were recorded on a JASCO J1500 spectropolarimeter with a 1 mm optical path length quartz cuvette at 25.0 ± 0.1 °C. Samples (R1 and S1) were dissolved in acetonitrile at 0.857 mg mL^{-1} (0.013 M as the concentration of the optically active repeating units) from 600 nm to 185 nm at a scan rate of 50 nm min^{-1}. Molar ellipticity was calculated using standard normalization procedures (SI, Section S1).

2.3.4. Differential scanning calorimetry (DSC) analysis

DSC experiments were conducted in a PerkinElmer 8500 calorimeter equipped with a refrigerated cooling system, Intracooler 3, under an ultrapure nitrogen atmosphere at a 20 mL/min flow rate. Samples (3–5 mg) were sealed in aluminum pans. The general procedure consisted of erasing thermal history by heating to $T_m + 30$ °C for 3 min, followed by controlled cooling/heating steps. Only the key conditions are listed below; full details appear in SI (Section S2).

2.3.4.1. Non-isothermal DSC scans. Samples were cooled from the melt to –40 °C at 20 °C/min, held isothermally for 1 min, and reheated at 20 °C/min. Melting/crystallization temperatures and enthalpies were extracted from the second heating and cooling scans.

2.3.4.2. Isothermal experiments. The minimum crystallization temperature ($T_{c,min}$) preventing crystallization during quenching (60 °C/min) was first determined following the Müller et al. protocol. [43] Isothermal experiments [43,44] were then conducted for $T_c \geq T_{c,min}$, and the resulting melting scans (after the isothermal step) were used for

Hoffman–Weeks extrapolation of the equilibrium melting temperature, T_m° (SI, Section S3).

2.3.4.3. Successive Self-nucleation and Annealing (SSA) thermal fractionation. SSA fractionation followed the standard Müller et al. [45–48] protocol. A qualitative scheme was used with $T_{s,ideal} = 65$ °C, identified via self-nucleation [49–52] experiments (SI, Section S4). Samples were fractionated across 5 °C windows covering the full melting range. The final heating scan displayed the resulting lamellar populations. The complete SSA step sequence is provided in the SI (Section S4).

2.3.5. Wide-Angle X-ray scattering (WAXS) and Small-Angle X-ray scattering (SAXS)

Simultaneous WAXS/SAXS measurements were carried out at the BL11-NCD beamline (ALBA Synchrotron, Barcelona) using the same thermal protocol as non-isothermal DSC. Scattering profiles were collected continuously during cooling and heating. WAXS was employed to identify crystalline reflections and interplanar distances (*d*-spacings), while SAXS provided information on long periods and lamellar thicknesses. Detector configurations, acquisition rates, sample–detector distances, and calibration procedures are detailed in the SI (Section S2).

2.3.6. Polarized light optical microscope (PLOM) analysis

Spherulite development was observed using an Olympus BX51 microscope equipped with a Linkam TP-91 hot stage. Thin films (~10 μm) were prepared by melting between glass slides. Two sets of experiments were conducted: (i) Non-isothermal PLOM, where samples were crystallized from the melt at 20 °C/min; and (ii) Isothermal PLOM, where samples were quenched at 50 °C/min to the target T_c, with radius changes recorded over time to determine growth rates. Banding periodicity was measured from micrographs. Growth-rate data were fitted using the Lauritzen–Hoffman equation. Full imaging conditions are detailed in the SI (Section S5).

3. Results and discussion

3.1. Stereodefined PPO samples synthesized by oxyanionic polymerization from EG6 initiator

Isotactic polypropylene oxide (*i*PPO) samples were synthesized via oxyanionic polymerization of enantiopure (*R*)- or (*S*)-propylene oxide (PO), using hexaethylene glycol (EG6) as a difunctional initiator activated by a 1:1 mixture of potassium acetate and 18-crown-6 ether (KOAc/18C6).[53] Polymerizations were conducted under solvent-free conditions at room temperature, with an initial $[OH]_0/[KOAc/18C6]_0$ ratio of 2, and M_n was tuned in a controlled manner by adjusting the initial $[PO]_0/[EG6]_0$ ratio (37.5, 90, 190, and 365) (Table 1). At a low targeted degree of polymerization (*DP*), conversions reached 99 % within 2 days, whereas higher targeted M_n required up to 7 days. For comparison, a racemic PPO sample (*rac*-PPO) was synthesized under identical conditions, targeting a *DP* of 90($[PO]_0/[EG6]_0 = 90$). This racemic reference allows distinguishing purely stereoconfiguration effects from those derived from M_n variations.

A clear macroscopic difference was observed: *i*PPO samples precipitated as white powders, whereas *rac*-PPO remained a viscous oil, indicating the expected strong influence of tacticity on crystallinity (Fig. S1). Nuclear magnetic resonance (NMR) spectroscopy and size-exclusion chromatography (SEC) analyses confirmed successful polymerization and controlled chain growth (Table 1, Figs. S1 to S3). As expected, the M_n increased proportionally with the targeted *DP* ($[(X)\text{-}PO]_0/[EG6]_0$ ratio, with X = *R* or *S*), as shown in Table 1 and Fig. 1a. It is worth noting that the sample codes used in Table 1 (e.g., PPO-*R*-2.6 or PPO-*S*-11.6) indicate the enantiomeric form (*R* or *S*) followed by the M_n determined by ^{1}H NMR divided by 1000. The polymerizations remained well-controlled, yielding monomodal SEC traces with narrow dispersity values ($Đ_M < 1.1$) and a regular shift toward lower retention volumes over time (Fig. S3). To evaluate the dependence of crystallization parameters on molecular weight, the M_n values obtained from SEC were used, as these best reflect the effective molar mass distribution relevant to crystallization processes. Comparisons of relevant parameters as a function of M_n, based on NMR data, are provided in the SI. The resulting *rac*-PPO similarly exhibited a narrow molecular weight distribution ($Đ_M < 1.15$) and an $M_{n,SEC}$ of 6,500 g mol^{-1} (Fig. S1), closely matching those of isotactic PPO samples: PPO-*R*-5.5 and PPO-*S*-7.5, validating the reproducibility of the polymerization system. Wide-angle X-ray scattering (WAXS) patterns confirmed that the crystalline structure of the samples corresponds to that of the PPO unit cell (Table S1). Additionally, small-angle X-ray scattering (SAXS) patterns in the melt showed no signs of phase separation (Fig. S4), indicating that the materials are homogeneous and do not undergo microphase separation.

Table 1
Enantiomerically pure isotactic PPO samples initiated from EG6 and prepared using a 1:1:1 ratio of $[EG6]_0/[18C6]_0/[KOAc]_0$. [a] Determined by ^{1}H NMR spectroscopy using the $-CH_2CH(CH_3)OH$ proton on the terminal unit of the copolymers. [b] Determined by SEC calibrated with polystyrene (PS) standards at 35 °C.

R-Sample	$[(R)\text{-}PO]_0/[EG6]_0$	$M_{n,th}$ (g mol^{-1})	$M_{n,NMR}$ (g mol^{-1})[a]	$M_{n,SEC}$ (g mol^{-1})[b]	$Đ_M$[b]
PPO-*R*-2.6	37.5	2100	2630	3800	1.10
PPO-*R*-5.5	90	5200	5450	7320	1.09
PPO-*R*-9.5	190	11,000	9530	12,130	1.10
PPO-*R*-11.1	365	21,200	11,080	15,400	1.13
S-Sample	$[(S)\text{-}PO]_0/[EG6]_0$	$M_{n,th}$ (g mol^{-1})	$M_{n,NMR}$ (g mol^{-1})[a]	$M_{n,SEC}$ (g mol^{-1})[b]	$Đ_M$[b]
PPO-*S*-2.8	37.5	2100	2780	3800	1.07
PPO-*S*-7.5	90	5200	7540	7500	1.09
PPO-*S*-8.9	190	11,000	8886	10,200	1.09
PPO-*S*-11.6	365	21,200	11,600	12,500	1.09

^{13}C NMR spectroscopy provides clear evidence of the microstructural order in isotactic PPO samples. For example, the spectra of PPO-*R*-5.5 and PPO-*S*-7.5 show distinct and well-defined peaks at chemical shift (δ) of 73.58 ppm and $\delta = 75.71$ ppm, which correspond to the methylene and methine carbon environments in the $-O-CH_2-CH(CH_3)-O-$ repeat units arranged in meso (*m*) and meso–meso (*mm*) diads, respectively. This specific distribution confirms the ordered spatial arrangement of monomers along the isotactic structure. In contrast, the ^{13}C NMR spectrum of *rac*-PPO of similar chain length exhibits broadened peaks in the same spectral regions, with a mixture of meso (*m*) and racemic (*r*) diad sequences: *rrm* or *mrr* at δ of 73.09 ppm, *m* at 73.42 ppm, *rr* at 75.23 ppm, *mr* + *rm* at 75.47 ppm, and *mm* at 75.66 ppm. This complex pattern reflects a random distribution of stereocenters along the polymer chain, confirming the atactic nature of *rac*-PPO (Fig. S5).

Circular dichroism (CD) spectra were recorded in acetonitrile (ACN). This solvent ensures complete solubility of all polymer samples and provides a suitable UV cutoff for the high-energy absorption bands. The isotactic PPO samples: PPO-*R*-2.6 and PPO-*S*-2.8 exhibited strong, mirror-image CD signals with absorption maxima at ca. 190 nm (Fig. 1b), consistent with values reported for structurally related chiral ethers such as (S)-isobutyl ethyl ether in heptane solution.[54,55] These bands are attributed to $n \rightarrow \sigma^*$ transitions, characteristic of saturated molecules bearing lone pair-containing atoms. The racemic PPO, obtained by copolymerizing equimolar amounts of (*R*)- and (*S*)-PO, was CD-inactive as expected. The calculated molar extinction coefficients (ε, ca. 800 M^{-1} cm^{-1}) and the molar circular dichroism coefficient (Δε, ca. 1 M^{-1} cm^{-1}), based on the concentration of chiral PPO repeating units, are in good agreement with reported values for these monomeric

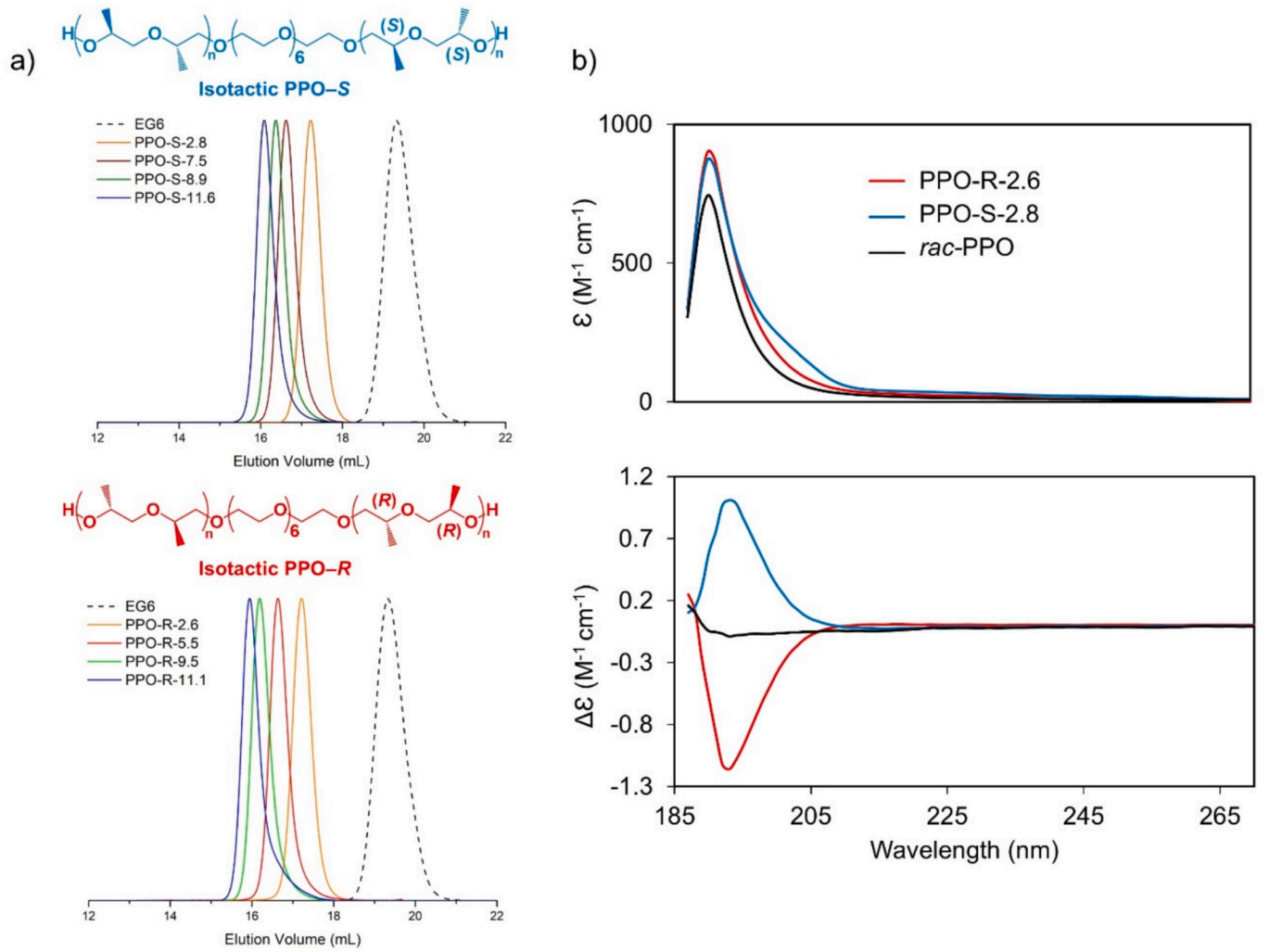

Fig. 1. a) SEC traces of EG6 initiator (dashed line) and corresponding isotactic PPO samples. b) UV and CD spectra of isotactic PPO samples (PPO-*R*-2.6 and PPO-*S*-2.8) and racemic PPO (*rac*-PPO) recorded in ACN.

analogues. Higher molar mass samples (PPO-*R*-11.1 and PPO-*S*-11.6) showed nearly identical spectral profiles, indicating that the CD response originates from the stereoregular configuration of the PPO chains rather than from long-range secondary structure formation.

3.2. Morphology and Spherulite growth (PLOM)

The effects of M_n and stereoconfiguration on PPO crystallization behavior were analyzed using PLOM, with a focus on morphological changes and spherulitic growth. As detailed in the SI (Section S5), all PPO samples, regardless of stereoconfiguration or M_n, formed well-developed negative spherulites during cooling from the melt at 20 °C/min (Fig. S17). This confirms that stereoconfiguration does not alter the qualitative spherulitic morphology under non-isothermal conditions.

The PPO spherulitic morphology was also examined under isothermal conditions (Fig. 2). All samples developed well-defined negative spherulites with Maltese-cross and banding extinction patterns. While the overall morphology is unaffected by stereoconfiguration, a systematic and reproducible difference was detected: PPO-*R* consistently showed a larger banding periodicity than PPO-*S* at all crystallization temperatures (Fig. S18). Since banding originates from lamellar twisting [56] and is highly sensitive to the asymmetry between the two crystal faces, this observation suggests that the helicoidal conformations adopted by PPO-*R* and PPO-*S* chains in the melt may not be perfectly equivalent, despite leading to enantiomorphic crystal lattices. In chiral polymers, slight differences in the stability or cooperativity of P (right-handed)- and M (left-handed)-type local helices [57,58] can influence the surface-stress imbalance that drives lamellar twisting. [59–62] Thus, the distinct banding periodicities likely reflect subtle melt-state conformational biases between the two enantiomers.

These melt-state differences provide a first indication that PPO-*R* and PPO-*S* are not dynamically equivalent, even though their crystalline unit cells are identical. Because lamellar banding is a melt-sensitive phenomenon, the observed disparity in pitch is consistent with the two enantiomers experiencing slightly different segmental mobilities or frictional environments before crystallization. As shown in the following sections, these differences are evident in both non-isothermal and isothermal crystallization kinetics, including a reproducible molecular-weight-dependent crossover in growth, nucleation, and overall crystallization rates.

The spherulitic growth rate (G) was determined under isothermal conditions by cooling the samples to selected T_c values between 7 and 45 °C (Fig. S19, SI Section S5).

Fig. 3 shows the G vs. T_c plots for all samples. In this figure, the solid lines represent the fit based on Lauritzen-Hoffman (LH) crystallization theory. [63] The parameters obtained are listed in Table S5. The experimental data only captured the secondary nucleation-dominated region of the typical bell-shaped crystallization window, [64–67] since at lower T_c, crystallization during cooling was too fast to measure, and at higher T_c, secondary nucleation was greatly reduced. [64–67] The

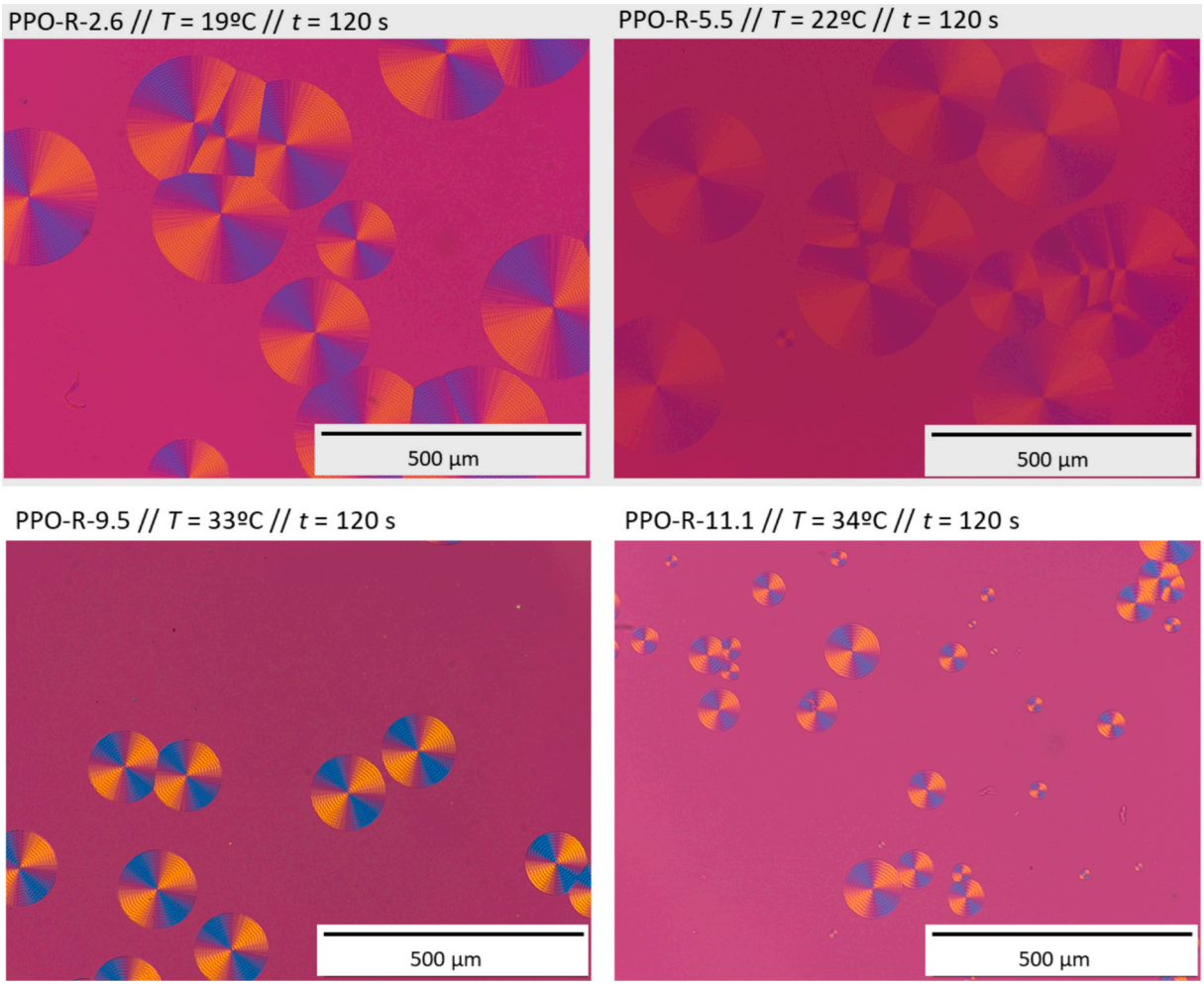

Fig. 2. PLOM representative micrographs for PPO samples. Micrographs were taken under isothermal conditions at the indicated T_c and after 120 s for all the samples.

extracted values from Figs. 3a and b are summarized in Table S6.

Figs. 3a and b show that increasing M_n systematically shifts the G-T_c curves to higher temperatures, particularly between the low-M_n (PPO-*R*-2.6, PPO-*S*-2.8) and intermediate-M_n samples (PPO-*R*-5.5, PPO-*S*-7.5). At high M_n, the shift becomes less pronounced, suggesting that the samples approach a near-plateau regime in which G is no longer strongly dependent on M_n. To better visualize these trends, G at constant T_c and T_c at constant G were plotted as a function of M_n (Figs. 3c and d).

Plotting G (at a constant T_c) (Fig. 3c and S20) or T_c (at a constant G) (Fig. 3d and S21) versus M_n clearly shows that higher M_n enhances secondary nucleation, leading to faster spherulitic growth (only the secondary nucleation part of the growth kinetics was experimentally accessible, i.e., the right-hand side of the growth rate versus T_c curve). As demonstrated by Okui et al. [68] and Mandelkern et al., [69] and more recently Fernández-Tena et al., [70] when the growth rate is plotted against molecular weight, it also forms a bell-shaped curve. However, in this case, the left-hand side of the curve is dominated by secondary nucleation, while the right-hand side is dominated by diffusion, since increasing M_n also increases the number of entanglements per chain, hindering the diffusion of chains to the growth front. Therefore, based on Fig. 3c, it is obvious that the range of molecular weights used in this work falls within the left side of the G versus M_n bell-shaped curve (determined at a constant T_c).

When the effect of stereochemistry is examined at constant T_c, a clear trend emerges. PPO-*R* shows faster growth than PPO-*S* at low M_n, with differences of approximately 0.15 µm/min (Fig. 3c). At higher M_n, however, this tendency becomes progressively less pronounced and eventually reverses, with PPO-*S* growing slightly faster by about 0.05 µm/min. A similar M_n-dependent behavior is observed when comparing T_c at constant G (Fig. 3d), where low-M_n PPO-*R* requires roughly 15 °C higher T_c than PPO-*S* to reach a given G. Conversely, at high M_n, PPO-*S* becomes the faster crystallizing.

Although modest in magnitude, this reproducible M_n-dependent inversion appears consistently across all measurements and therefore represents a robust experimental feature of the system. The experimental evidence suggests that stereoconfiguration may influence melt dynamics rather than crystalline structure, resulting in different crystallization behaviors at low and high M_n. As discussed later, we hypothesize that these effects may stem from differences in the onset of chain entanglements and subtle stereoconfiguration-dependent variations in segmental mobility in the melt.

3.3. Non-isothermal DSC

After evaluating the morphological changes and spherulitic growth under non-isothermal conditions, the thermal transitions were analyzed using DSC with the same cooling and heating protocol. Fig. 4 displays the cooling (Figs. 4a and c) and second heating (Figs. 4b and d) DSC scans for PPO-*R* (Figs. 4a and b) and PPO-*S* (Figs. 4c and d) with different M_n. All samples show a single crystallization peak during

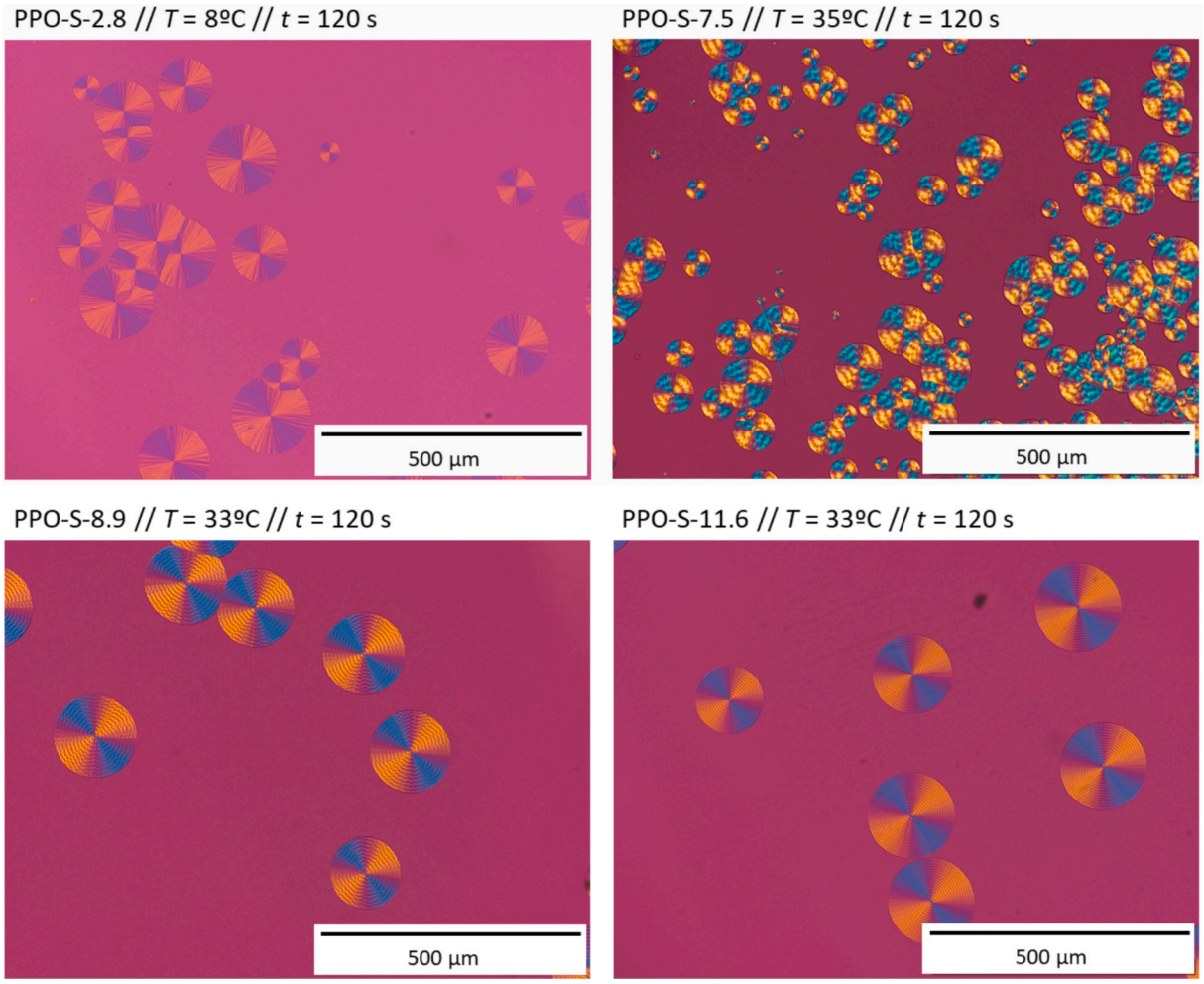

Fig. 2. (*continued*).

cooling, which shifts systematically with M_n and stereoconfiguration. During heating, a small exothermic event occurs just before melting, attributed to recrystallization, confirmed by WAXS/SAXS evidence of structural reorganization at low temperatures (Figs. S6 and S7). All thermal transition data, including melting and crystallization temperatures and enthalpy (used to calculate the degree of crystallinity, X_c, as shown in Equation S1), are summarized in Table S2.

Fig. 5 compares T_c and T_m as a function of M_n. Comparisons of the X_c as a function of M_n are made in Fig. S8 (see details in the SI, Section S2) and Fig. S15 (under isothermal conditions). The T_c variation with M_n (Fig. 5a) shows a clear trend: T_c increases with M_n until approaching a plateau, reflecting the secondary nucleation control at low M_n values. As M_n decreases, nucleation becomes more difficult because shorter chains have greater mobility and detach more easily when forming a stable nucleus. As chain length increases, the chains are stabilized faster as they form a secondary nucleus. Although catalytic residues or minor heterogeneities may influence absolute T_c values, the consistent M_n-dependent trend across samples allows reliable comparison. Interestingly, PPO-*R* reaches its T_c plateau at lower M_n than PPO-*S*, a trend that is consistent with the inversion identified in PLOM (banding periodicity) and growth-rate measurements and is therefore compatible with the idea that stereoconfiguration may influence crystallization primarily through melt-related factors rather than crystalline structure.

A more robust parameter, less sensitive to heterogeneities, is T_m. Fig. 5b shows that T_m increases significantly at low M_n for both PPO-*R* and PPO-*S*, then gradually levels off at higher M_n, mirroring the trend seen in PLOM. At the highest M_n, T_m values for PPO-*R* and PPO-*S* converge, consistent with previous research on PPO [71] and other semicrystalline polymers: PCL [70], PE [72], and PHB [73]. For PPO-*R*, the T_m increases by about 10 °C across the M_n series, while for PPO-*S* it rises by roughly 20 °C. This difference indicates that stereoconfiguration may affect how crystalline stability depends on M_n, in line with previous trends seen in T_c and G versus M_n. Overall, both PPO-*R* and PPO-*S* crystallize more easily as M_n increases, but the extent and starting point of this improvement vary slightly between enantiomers, again suggesting a melt-state rather than a lattice-level effect.

The combined T_c and T_m results are consistent with a dynamic origin for the stereoconfiguration effects. PPO-*R* and PPO-*S* form identical unit cells, yet their melt-state mobilities, and thus their crystallization rates, may well vary depending on M_n. As discussed in the next section, SSA experiments further confirm that these differences remain under controlled thermal fractionation conditions.

3.4. *Successive self-nucleation and annealing (SSA)*

To complement the non-isothermal DSC analysis and assess the crystalline populations under conditions closer to thermodynamic equilibrium, SSA experiments were conducted following the protocol established by Müller et al. [45–48]. SSA induces progressive lamellar thickening through alternating heating and cooling cycles, enabling comparison of the thermal fractionation capacity across samples. A qualitative fractionation protocol was chosen, using a single $T_{s,ideal}$ = 65 °C, the highest ideal self-nucleation temperature among all materials identified via SN experiments (SI, Section S4), to ensure consistent

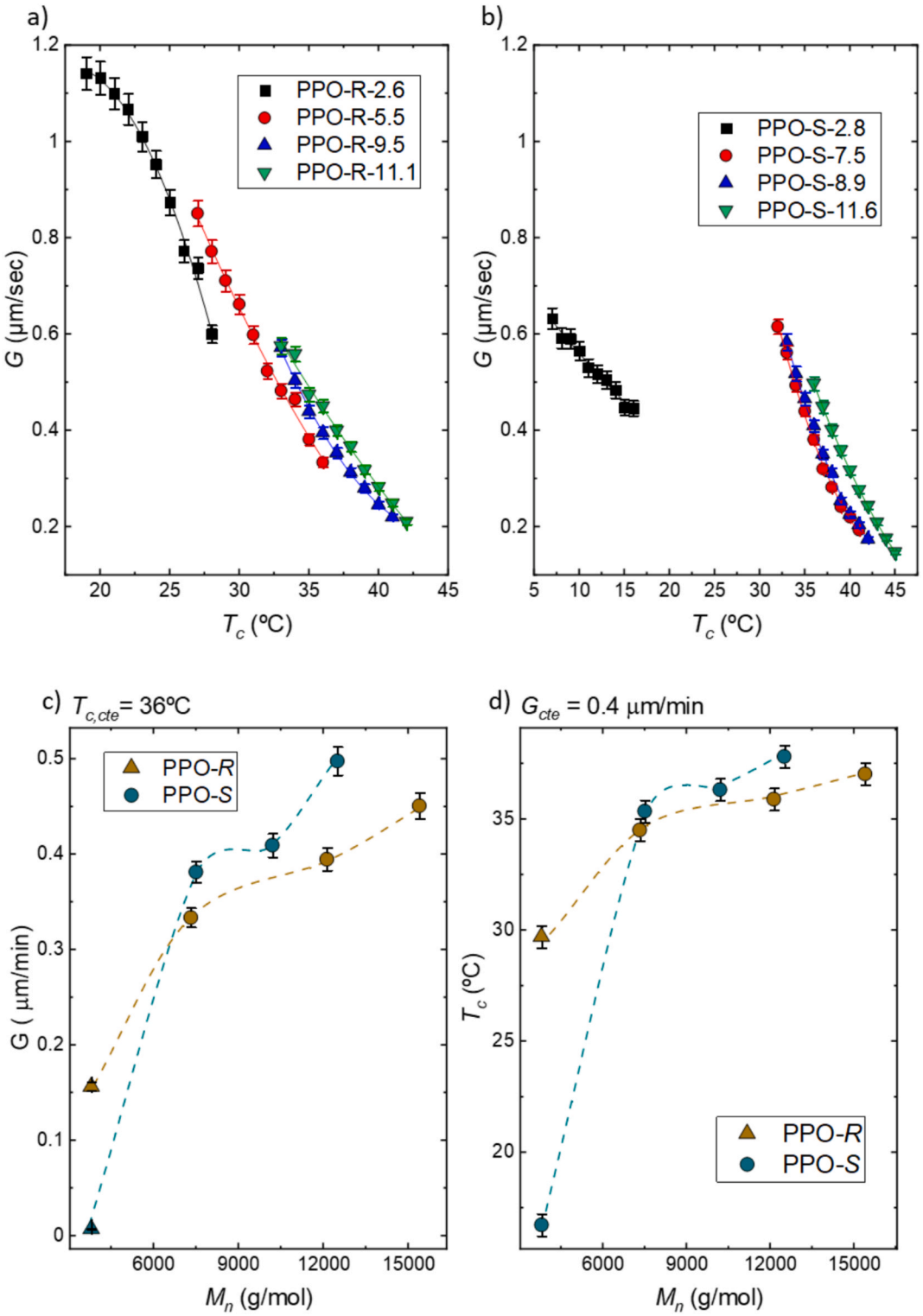

Fig. 3. Spherulitic growth rate (G) of a) PPO-*R* and b) PPO-*S* samples as a function of crystallization temperature. c) G value of PPO-*R* and PPO-*S* samples as a function of molecular weight at $T_c = 36$ °C. d) T_c value of PPO-*R* and PPO-*S* samples as a function of molecular weight at a constant G value ($G = 0.4$ µm/min). The solid lines in a) and b) are fits to the Lauritzen and Hoffman equation. The dashed line in c) and d) is a line to guide the eye. In c) and d), the triangle symbols represent extrapolated values, and the circle symbols represent measured data points. Error bars correspond to the standard deviation of G values obtained from measurements on 5 or more independent spherulites.

comparison, along with a fractionation window of 5 °C covering the entire melting range of all samples.

Fig. 6 shows the final DSC heating scans after the SSA treatment for all samples. Vertical lines mark the T_s values, and the segmented line indicates the initial T_s of the procedure, i.e., the $T_{s,ideal}$. The melting peaks are labeled according to their origin. Melting peak 1 corresponds to an annealed population mainly produced during the 5 min at $T_{s,1}$. Melting peak 2 forms at $T_{s,2}$, and so on. These fractions come from the

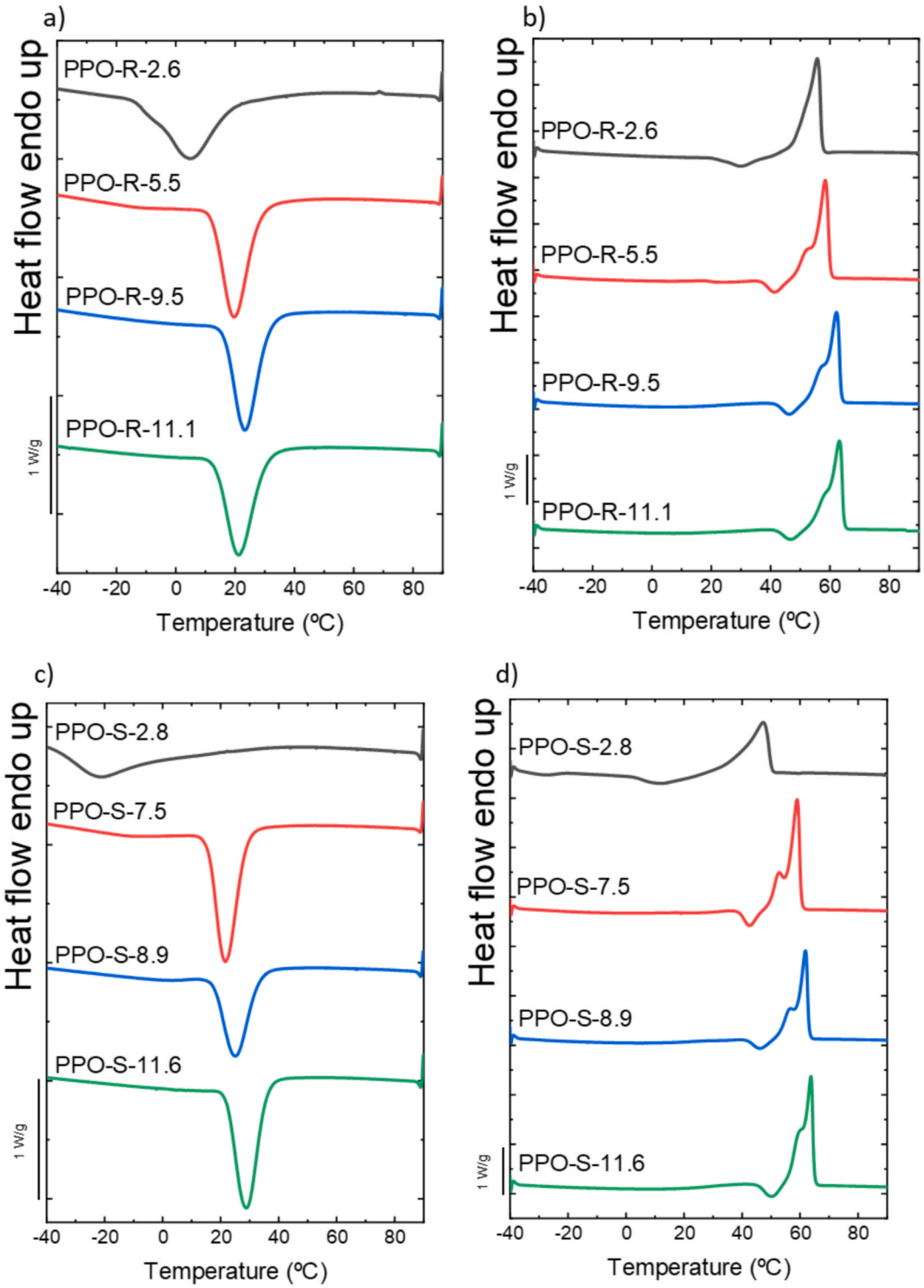

Fig. 4. DSC cooling (a,c) and heating (b,d) scans at 20 °C/min for PPO-*R* (a and b) and PPO-*S* (c and d) samples.

molecular weight distribution and, importantly, from intermolecular interactions that result in different crystal stabilities, consistent with the behavior recently reported by Sangroniz et al. [74].

All PPO samples, regardless of stereoconfiguration, exhibited qualitatively similar SSA profiles and the same number of fractions. However, subtle and reproducible stereoconfiguration-dependent effects were observed, fully consistent with the melt-state differences inferred from PLOM and DSC. First, the fractionation quality, evaluated by the relative sharpness and separation of the fractions, was higher for PPO-*S* at low M_n than for PPO-*R* of similar M_n. The better-defined fractions in PPO-*S* suggest enhanced lamellar thickening or chain mobility during annealing at low M_n. At high M_n, the SSA profiles of PPO-*R* and PPO-*S* became more similar. Furthermore, although PPO-*R*-2.6 and PPO-*S*-2.8 have comparable M_n, fraction 2 appears at a higher temperature for PPO-*R*, indicating that PPO-*R* chains produce slightly thicker or more stable lamellae under identical annealing conditions. This observation is consistent with possible melt-dynamics differences inferred from PLOM and DSC: at low M_n, PPO-*R* exhibits faster crystallization and an earlier

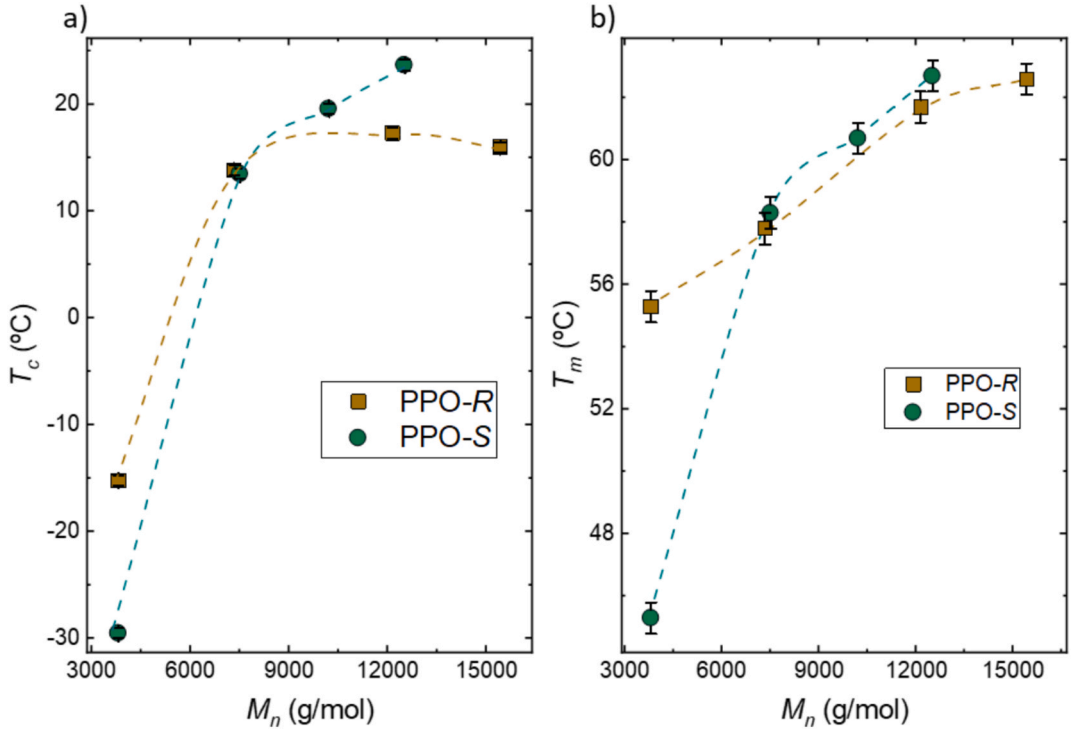

Fig. 5. A) T_c and b) T_m as a function of the M_n of the PPO samples. Error bars indicate a conservative temperature uncertainty of ± 1 °C, chosen to exceed the maximum instrumental error of the DSC apparatus (±0.5 °C).

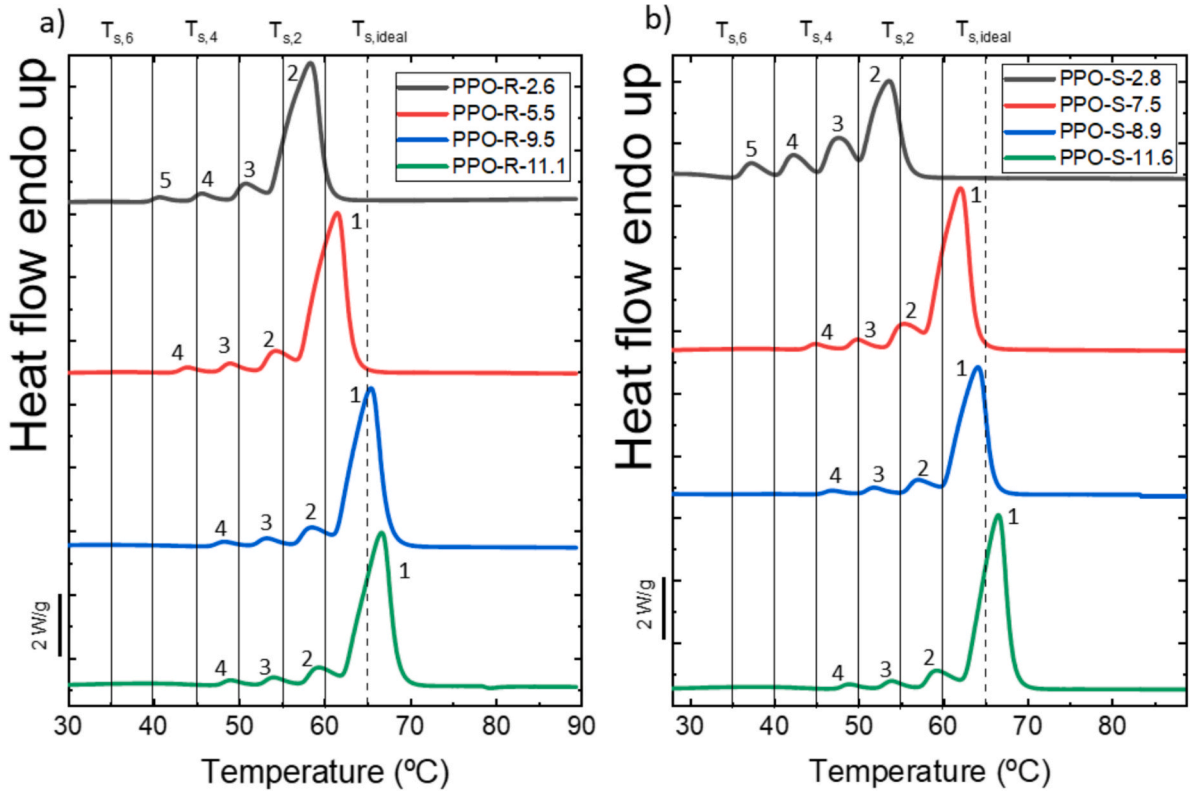

Fig. 6. Final DSC heating scans after SSA thermal fractionation for a) PPO-*R* and b) PPO-*S* samples.

onset of crystallinity enhancement. The agreement across techniques is therefore consistent with the view that stereoconfiguration may influence crystallization through melt dynamics rather than differences in crystalline structure.

Regarding the M_n effect, both PPO-*R*-2.6 and PPO-*S*-2.8 lack fraction 1 because $T_{s,1}$ is above their effective melting range; the first fraction appears only at $T_{s,2}$. As M_n increases, fraction 1 becomes clearly visible, indicating that longer chains form thicker lamellae capable of surviving

conditioning at $T_{s,1}$. This trend is consistent with the expected molecular-weight dependence of lamellar stability observed in other semicrystalline polymers. [70,75].

Plotting the melting point of the fraction that melts at the highest temperature, $T_{m,\ SSA}$, as a function of the M_n (Fig. S16) yields a trend remarkably similar to T_m vs. M_n (Fig. 5b). Likewise, comparison of T_m, $T_{m,SSA}$, and T_m° (estimated using the Hoffman-Weeks extrapolation, see Fig. S9 and Section S3 in the SI) as a function of the M_n (Fig. S10) demonstrates that the M_n effect prevails even under conditions closer to thermodynamic equilibrium (i.e., after SSA). Importantly, both enantiomers exhibit parallel M_n-dependent trends, indicating that stereoconfiguration does not alter the crystalline unit cell but may subtly modulate the melt-state mobility that determines lamellar stability during annealing.

3.5. Study of the overall crystallization kinetics by DSC

To complement the PLOM growth-rate analysis and the SSA fractionation results, the overall crystallization kinetics were studied by isothermal DSC. This technique provides access to kinetic parameters, such as the induction time (t_0) and the overall half-crystallization time ($\tau_{50\%}$), which reflect the combined contributions of nucleation and growth. The experimental data obtained were analyzed using the Avrami [76,77] and LH [63] theories (Eqs. S2 (Section S3), S3 and S4 (Section S5) in the SI for more details).[44,63] To apply them, the recently updated Crystallization Fit Origin® app, based on the plug-in

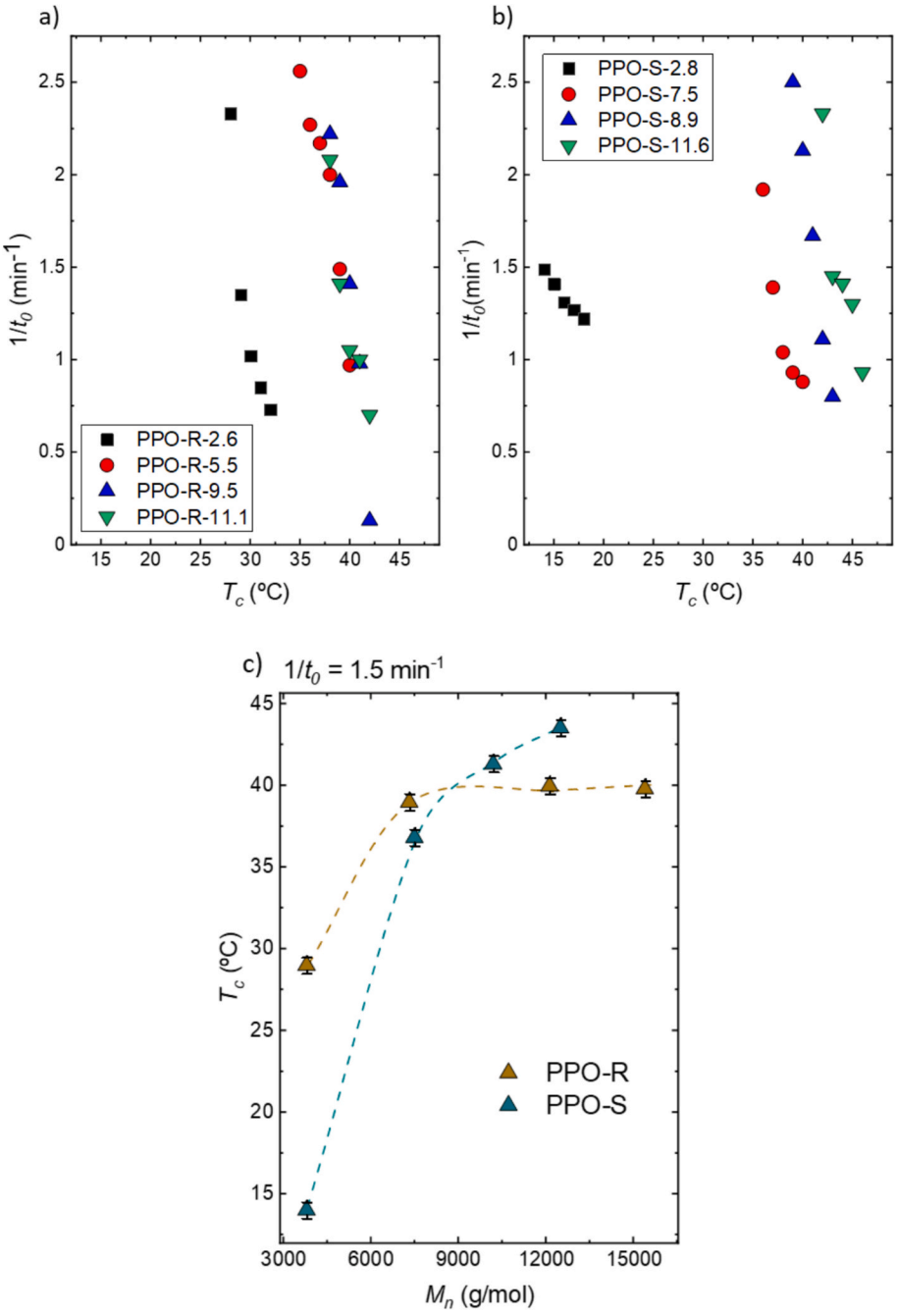

Fig. 7. Inverse of induction time ($1/t_0$) as a function of T_c for a) PPO-*R* and b) PPO-*S* samples. c) Crystallization temperature as a function of M_n at a constant value of $1/t_0 = 1.5$ min $^{-1}$ for PPO-*R* and PPO-*S* samples. Error bars indicate a conservative temperature uncertainty of ± 1 °C, chosen to exceed the maximum instrumental error of the DSC apparatus (±0.5 °C).

developed by Lorenzo et al. [44] and reviewed by Pérez-Camargo et al. [43] was used. The parameters obtained from this analysis allow quantitative comparison of the crystallization behavior of PPO-*R* and PPO-*S* across the M_n series.

Representative isothermal crystallization exotherms and Avrami fits (Section S3) are provided in the Supporting Information (Fig. S11). The sigmoidal profiles were fitted using the integrated Avrami equation, from which t_0 and $\tau_{50\%}$ were extracted. The Avrami exponent n ranged between 2.1 and 2.6 for all samples, indicating in most cases ($n > 2.4$) three-dimensional spherulitic growth with sporadic or instantaneous nucleation, consistent with PLOM observations. In addition, $k^{1/n}$, expressed in min^{-1}, shows a very similar trend to the inverse of $\tau_{50\%}$, i.e., the overall crystallization rate, $1/\tau_{50\%}$, as shown below, highlighting the accuracy of the Avrami fitting (Table S3).

Analyzing the isothermal curves through the Avrami fit, the induction time, t_0 (primary nucleation period before DSC can detect any

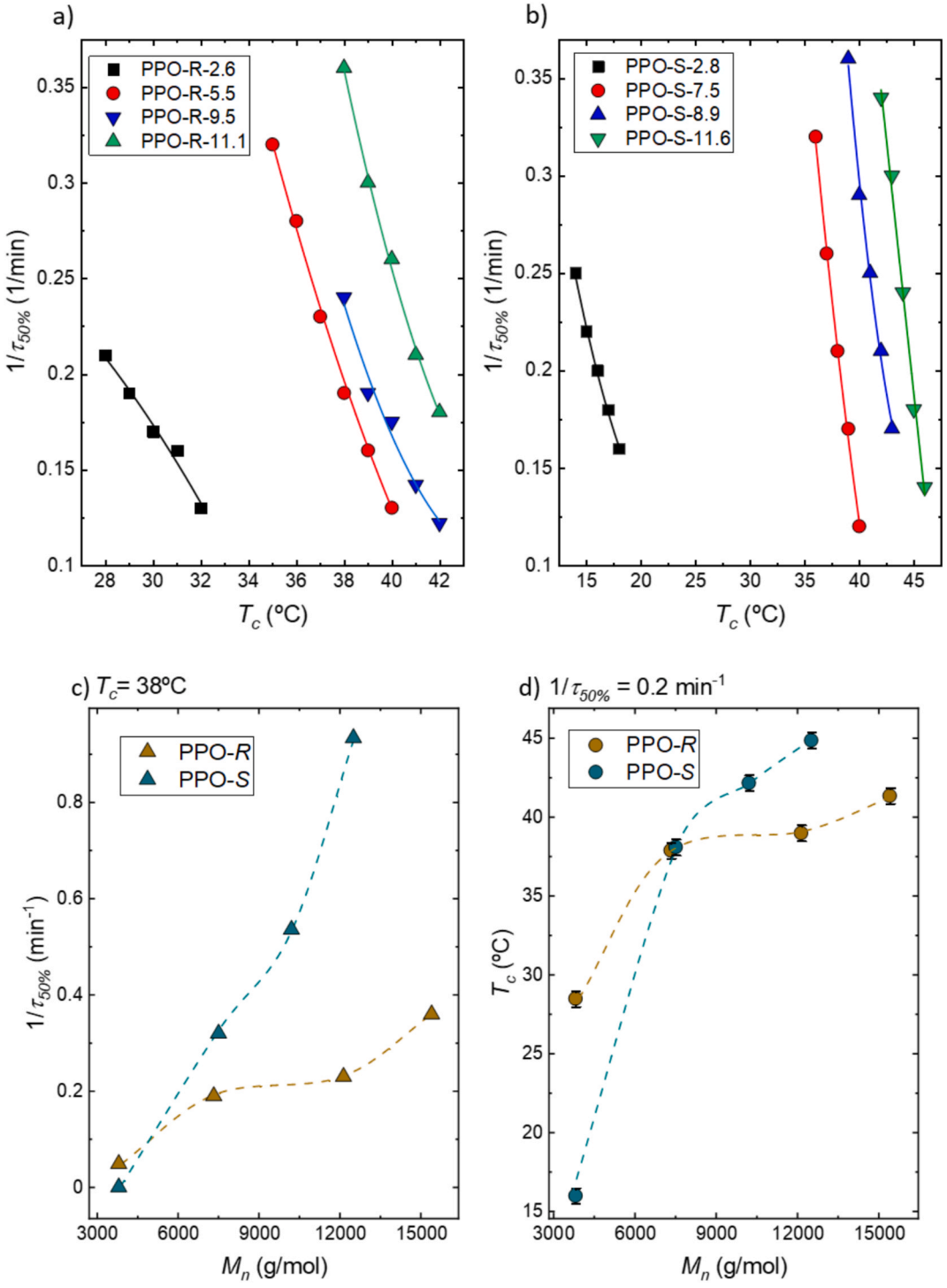

Fig. 8. Inverse of half crystallization time ($1/\tau_{50\%}$) as a function of T_c, for a) PPO-*R* and b) PPO-*S* samples. c) $1/\tau_{50\%}$ value of PPO-*R* and PPO-*S* samples as a function of molecular weight at $T_c = 38$ °C. d) T_c value of PPO-*R* and PPO-*S* samples as a function of molecular weight at a constant $1/\tau_{50\%}$ value ($1/\tau_{50\%}$ =0.2 μm/min). In c) and d), the triangle symbol represents extrapolated values, and the circle symbol represents non-extrapolated values. Error bars indicate a conservative temperature uncertainty of ± 1 °C, chosen to exceed the maximum instrumental error of the DSC apparatus (±0.5 °C).

significant calorimetric event, corresponding to the elapsed time for primary nucleation before crystal growth can be observed, as detailed by Pérez-Camargo et al. [43] and other works [73]) is obtained. The inverse of the induction time ($1/t_0$) is proportional to the primary nucleation rate before crystal growth begins. Figs. 7a and b show $1/t_0$ as a function of T_c for PPO-*R* (Fig. 7a) and PPO-*S* (Fig. 7b) of different M_n. As expected, $1/t_0$ decreases with increasing T_c across all the PPO samples since primary nucleation decreases as chain mobility increases at higher crystallization temperatures (or lower ΔT). From Figs. 7a and b, a constant $1/t_0$ value was selected to evaluate the M_n dependency, as shown in Fig. 7c. These results show that $1/t_0$ values increase with increasing M_n and that a trend toward a plateau is observed, as seen with the PPO-*R* sample, which, as expected, resembles the T_c vs M_n plot. Importantly, the stereoconfiguration dependence is fully consistent with the trends identified in PLOM, non-isothermal DSC, and SSA: at low M_n, PPO-*S* requires a larger supercooling (lower T_c) to match the nucleation rate of PPO-*R*, whereas at high M_n, this trend reverses. This confirms that the *R* → *S* inversion is not technique-dependent but a robust feature of the crystallization kinetics.

This crossover in primary nucleation rate provides additional evidence for our hypothesis that stereoconfiguration subtly affects melt mobility. Because primary nucleation is highly sensitive to the efficiency

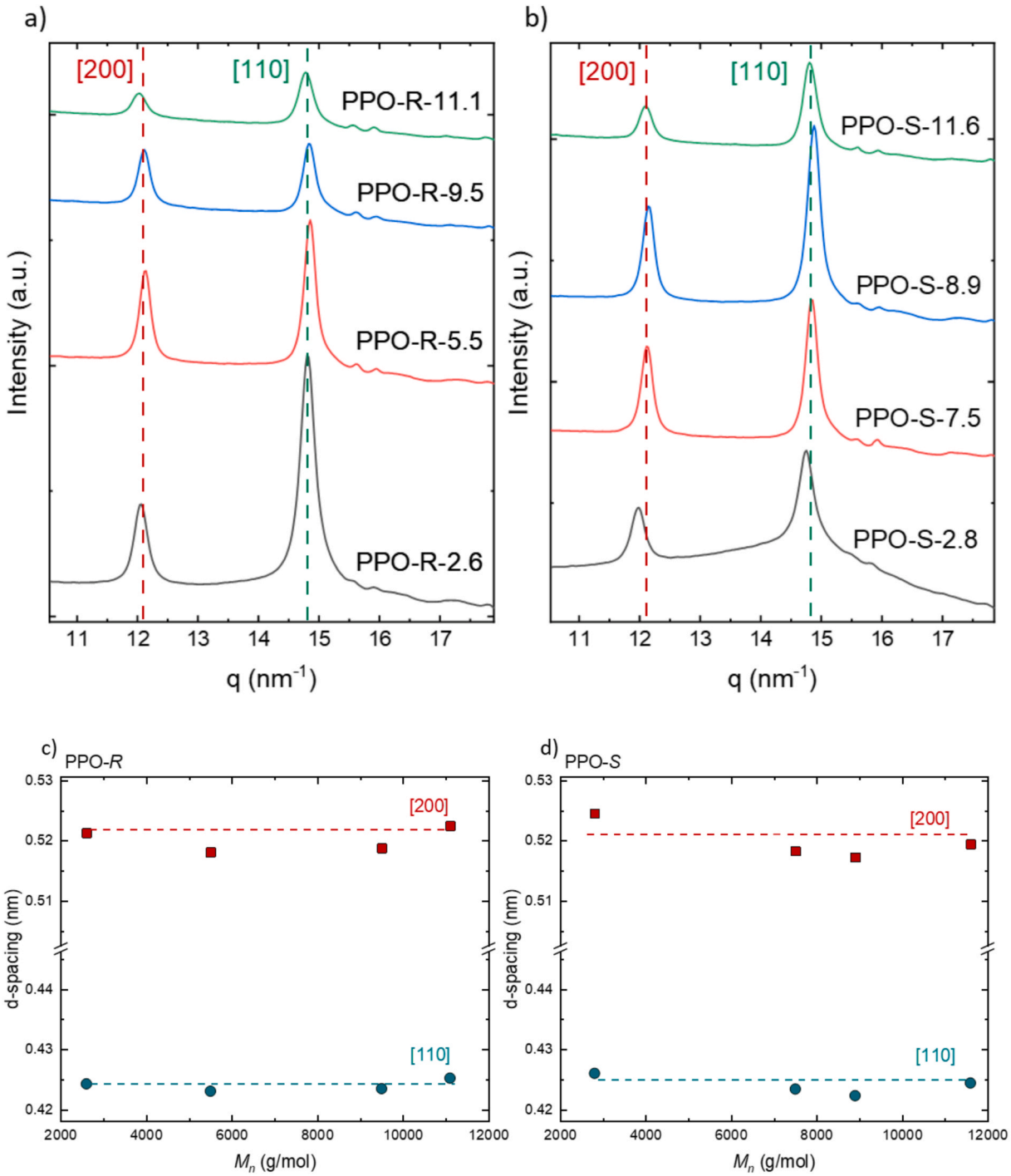

Fig. 9. WAXS diffractograms at −40 °C after cooling from the melt at 20 °C/min of a) PPO-*R* and b) PPO-*S* samples. Interplanar distances (*d*-spacing) of the indicated planes as a function of the molecular weight for c) PPO-*R* and d) PPO-*S* samples.

with which chains diffuse toward the heterogeneous substrate responsible for nucleation (e.g., catalytic residues), even small differences in segmental friction or local conformational preferences between the enantiomers can produce measurable kinetic asymmetries. This interpretation is also consistent with the melt-state differences inferred from banding periodicity and SSA fractionation.

In addition to $1/t_0$, the inverse of the overall half-crystallization time ($1/\tau_{50\%}$) was obtained to evaluate the overall crystallization rate. The experiemental $1/\tau_{50\%}$ values were fitted using the LH theory [63] (Equation S3), and the relevant parameters are summarized in Table S4. Figs. 8a and b demonstrate that increasing M_n systematically shifts the $1/\tau_{50\%}$ vs. T_c curves to higher temperatures, indicating faster crystallization, fully consistent with the results of G vs. T_c and $1/t_0$ vs. T_c.

Figs. 8c, d, S13, and S14 further confirm that PPO-*R* crystallizes faster at low M_n, whereas PPO-*S* becomes faster at high M_n, whether analyzed at constant T_c (Fig. 8c) or constant $1/\tau_{50\%}$ (Fig. 8d). The excellent agreement between nucleation, growth, overall crystallization rate, and non-isothermal transitions indicates that the stereoconfiguration effects are detectable throughout the entire crystallization process. The coherence across techniques also supports a melt-dynamic origin for the $R \leftrightarrow S$ inversion, rather than differences in crystalline packing. However, alternative contributions cannot be fully ruled out. Furthermore, the LH results listed in Table S4 illustrate how the energetic barrier for overall crystallization, K_g^{τ}, varies with M_n and stereoconfiguration, aligning with the experimental findings.

3.6. In situ WAXS/SAXS real-time synchrotron results

WAXS and SAXS measurements were carried out to evaluate whether the stereochemical differences between PPO-*R* and PPO-*S* produce any structural changes at the crystal or lamellar level. All measurements followed the same thermal protocol used in DSC, enabling direct comparison between techniques.

Figs. 9a and b show the WAXS patterns collected at −40 °C after cooling from the melt at 20 °C/min for PPO-*R* and PPO-*S* systems, respectively. All diffractograms exhibit the characteristic reflections of the orthorhombic PPO crystal structure, i.e., two main reflections at $q =$ 12.0 and 14.8 nm^{-1} from the planes (2 0 0) and (1 1 0) of an orthorhombic unit cell with the following dimensions: $a = 10.40$ Å, $b = 13.30$ Å, and $c = 5.96$ Å [21], with no detectable differences in peak positions, intensities, or interplanar distances (d-spacings, Figs. 9c and 9d), between the two enantiomers. This confirms that PPO-*R* and PPO-*S* crystallize into the same unit cell, indicating that stereoconfiguration does not alter the crystalline lattice, as occurs in other polymers, as PLLA and PDLA. [31] The full set of peak positions, d-spacings (Figs. 9c and 9d), and unit-cell parameters is reported in Table S1. The absence of peak splitting or secondary reflections indicates that the stereoconfiguration effects identified in PLOM, DSC, and SSA do not arise from structural polymorphism or crystal packing differences.

SAXS patterns show negligible changes in stereoconfiguration and M_n (see Figs. S22a and S22b). Moreover, the long period and lamellar thickness present similar values across different M_ns and stereoconfigurations (Fig. S23). Thus, neither lamellar spacing nor overall superstructure dimensions are affected by chain handedness.

Overall, the WAXS/SAXS results confirm that the crystalline unit cell and lamellar structure are unaffected by stereoconfiguration, consistent with the enantiomorphic nature of PPO-*R* and PPO-*S*. When combined with DSC, PLOM, and SSA, these findings indicate that the observed differences in crystallization kinetics most likely originate from melt-state phenomena rather than from solid-state structural variations. Notably, the M_n-dependent inversion in growth rates and the systematic differences in banding periodicity suggest that PPO-*R* and PPO-*S* may not be dynamically equivalent in the melt.

These trends suggest that chain handedness may subtly influence the stability and cooperativity of P- and M − type helical conformations, leading to minor differences in segmental friction or local packing before crystallization. Additionally, small stereoconfiguration-dependent variations in the effective molecular weight of entanglement may affect the onset of entanglement-controlled dynamics, thereby influencing nucleation and growth rates. Although further rheological and spectroscopic studies are needed to clarify the mechanistic details, the current results offer the first direct evidence that enantiomeric PPO chains can exhibit distinct melt behaviors even when crystallizing into identical lattices. These experimental findings open a promising path for future research into chirality-dependent melt dynamics and crystallization in stereoregular polyethers and related materials.

3.7. PPO-R:S blends

To evaluate whether mixing enantiomeric pairs affects crystallization, racemic PPO-*R*:*S* blends were prepared from PPO-*R* and PPO-*S* samples of comparable M_n. These blends enable the decoupling of the stereoconfiguration effect from the M_n effect, while allowing comparison with well-known racemic systems.

Fig. 10 shows the non-isothermal DSC cooling and heating scans for PPO-*R*:*S* samples alongside those of their enantiopure counterparts. The blends exhibit lower T_c and T_m than either PPO-*R* or PPO-*S* at the same M_n. This depression reflects reduced chain regularity within crystallizable segments, consistent with packing frustration most likely arising from the mixing of opposite helical senses. No new melting endotherms were observed, confirming that PPO-*R*:*S* blends do not form stereocomplexes or alternative crystalline phases. Despite a weak exothermic shoulder appearing near 40 °C during cooling, suggesting limited stereoselective interactions between the two helicities, the absence of new reflections in the WAXS patterns (Fig. S24) confirms that no stable stereocomplex is formed. The T_m value of PPO-*R*:*S* agrees with that reported in the literature for similar M_ns[78] confirming the absence of stereocomplex when PPO-*R* and PPO-*S* are blended.

At low M_n (Fig. 10a), the T_c of the blend falls between those of PPO-*R* and PPO-*S*, while at high M_n (Fig. 10b), it drops slightly below both, indicating slower overall kinetics. During heating (Figs. 10c,d), a cold-crystallization exotherm emerges only for the low-M_n blend, again indicating that opposite helicities partially disrupt chain organization, making crystallization less efficient in the mixed-chirality system.

WAXS and SAXS analyses (Figs. S24 and S25) show diffraction patterns identical to those of the enantiopure PPOs, with d-spacings of 0.52 nm (200) and 0.42 nm (110) remaining constant across compositions. The long period is likewise unaffected, demonstrating that the blends retain the same orthorhombic lattice as PPO-*R* and PPO-*S*. No microphase separation was detected, confirming full miscibility at the nanoscale. Thus, the crystallization retardation observed in PPO-*R*:*S* blends is compatible with packing frustration in the melt rather than from changes in crystalline symmetry or lamellar architecture.

PLOM observations (Fig. S26) reveal that the racemic blends form negative, non-banded spherulites, consistent with previous reports, [28,32]whereas the enantiopure PPOs occasionally exhibit banded textures. The G increases with M_n as expected (Figs. 11a and b), but the blend consistently shows slower growth than either PPO-*R* or PPO-*S* at the same T_c. Figs. 11c and d summarize this trend, illustrating the systematic reduction of G at constant T_c and T_c at constant G as a function of M_n upon mixing the two enantiomers. This behavior is fully consistent with the decrease in T_m and T_c seen in DSC, supporting the view that chirality mixing hinders lamellar assembly.

To quantify these effects, isothermal DSC experiments were performed. Fig. 12 compiles the $1/t_0$ and $1/\tau_{50\%}$ as functions of T_c. In all cases, the PPO-*R*:*S* blends exhibit lower $1/t_0$ and $1/\tau_{50\%}$ values than the corresponding enantiomers, confirming slower nucleation and overall crystallization. At a fixed rate, the blends require greater supercooling (Figs. S27 and S28), consistent with reduced nucleation efficiency and slower chain transport in the mixed-helicity melt.

This kinetic retardation may arise from packing frustration between chains of opposite helical senses, which could disrupt the local

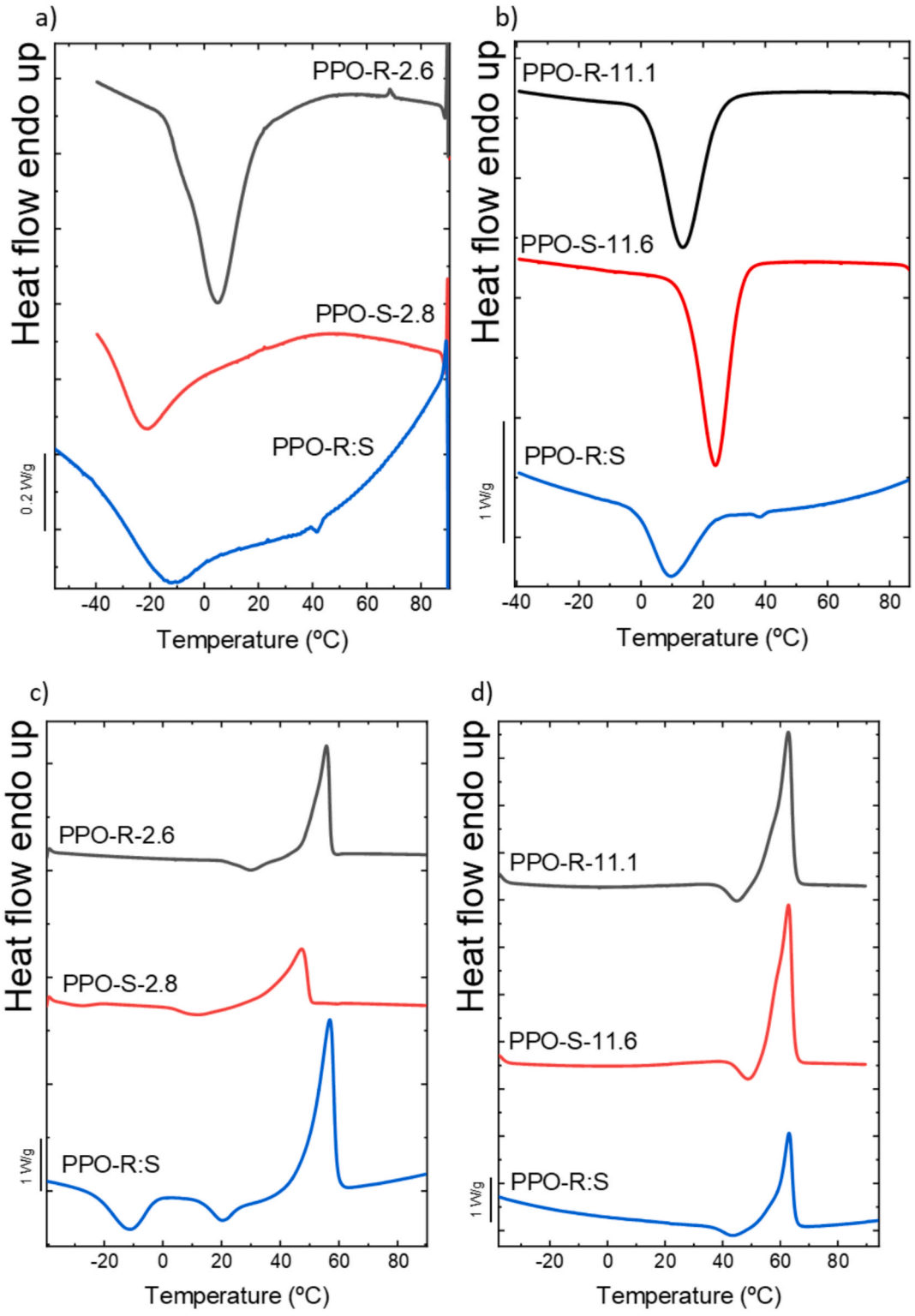

Fig. 10. DSC cooling scans at 20 °C/min for a) low M_n and b) high M_n and the subsequent DSC heating scans at 20 °C/min for c) low M_n and d) high M_n.

conformational coherence required for efficient chain folding. The behavior parallels that observed in PHB-*R*:*S* systems [73], where the opposite enantiomer disrupts packing and lowers T_m and T_c, whereas in PLLA/PDLA cooperative interactions promote the formation of highly stable stereocomplex crystals. PPO-*R*:*S* therefore represents an intermediate case where chirality neither produces cooperative stabilization nor new crystalline forms but instead subtly impedes the organization of like-handed chains.

These results show that enantiomeric mixing in PPO provides a simple means of tuning crystallization kinetics without altering crystal structure. By adjusting the *R*:*S* ratio or M_n, crystallization can be deliberately slowed, an advantageous property for processing or blending with biodegradable polymers such as PLA, where reduced crystallization rates can enhance optical clarity and broaden the processing window.

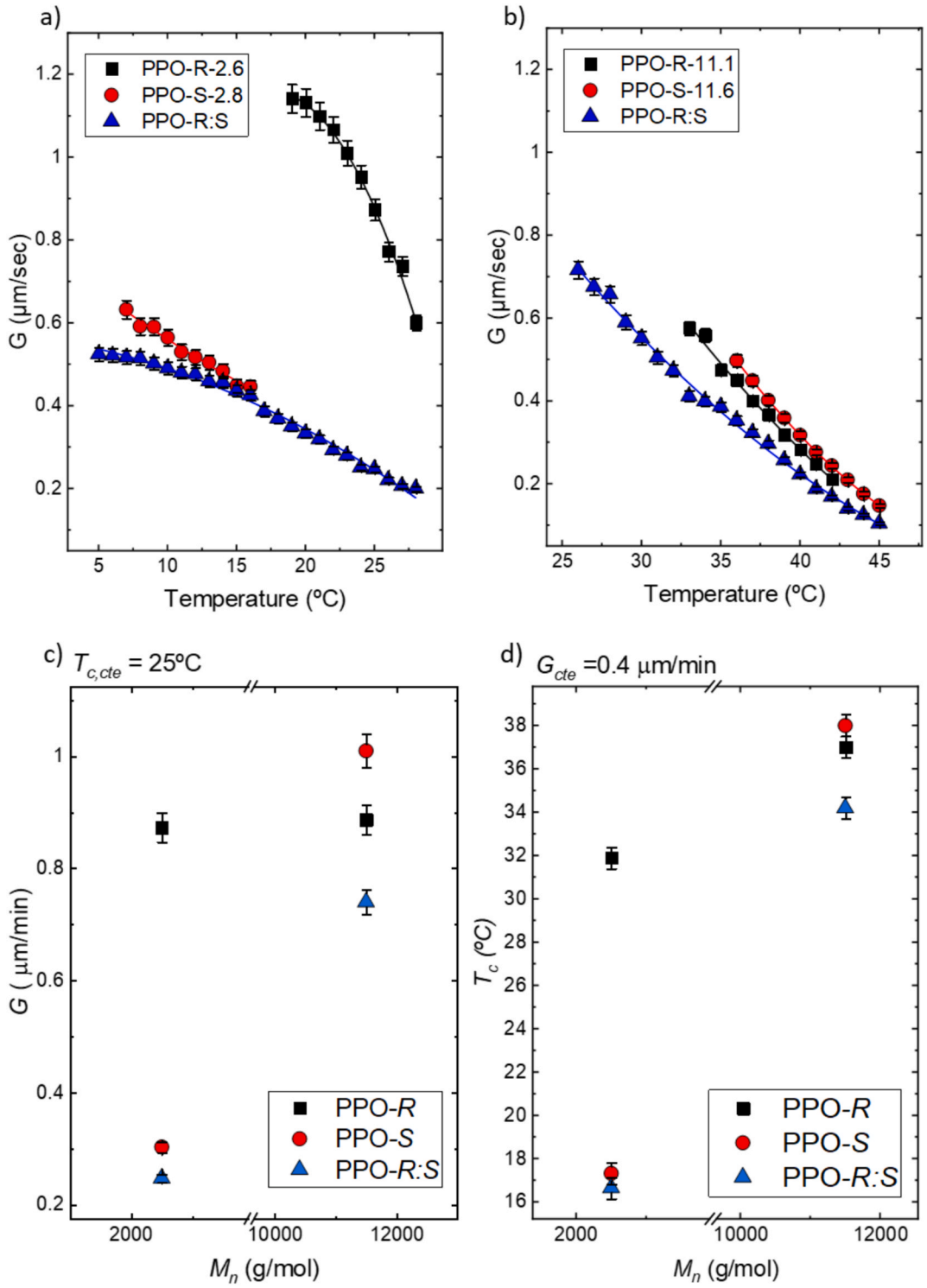

Fig. 11. Spherulitic growth rate (G) for a) low M_n and b) high M_n PPO-*R*:*S*, PPO-*R* and PPO-*S* samples as a function of crystallization temperature. In c) and d) comparisons of c) the G (at a constant T_c) and d) T_c (at a constant G) as a function of M_n are made for all samples. Error bars correspond to the standard deviation of G values obtained from measurements on 5 or more independent spherulites.

4. Conclusions

This study comprehensively analyzed PPO-*R*, PPO-*S*, and racemic PPO-*R*:*S* blends comprising 50 % *R* and *S* chains with varying M_n s through morphological, thermal, and structural characterization. Building on a previously reported catalytic system, we extended the scope of the oxyanionic polymerization of PO to include enantiopure monomers, enabling access to PPO-*R* and PPO-*S* with tunable molar masses. To ensure controlled initiation, hexaethylene glycol (EG6) was used as an initiator, without significantly impacting the properties of the resulting PPO. This approach enabled the synthesis of telechelic PPO samples across a broad M_n range for both enantiomeric series, as well as racemic blends by combining PPO-*R* and PPO-*S* of comparable M_n.

As M_n increases, both PPO-*R* and PPO-*S* samples exhibit increased crystallization and melting temperatures, higher nucleation and spherulitic growth rates, and faster overall crystallization kinetics,

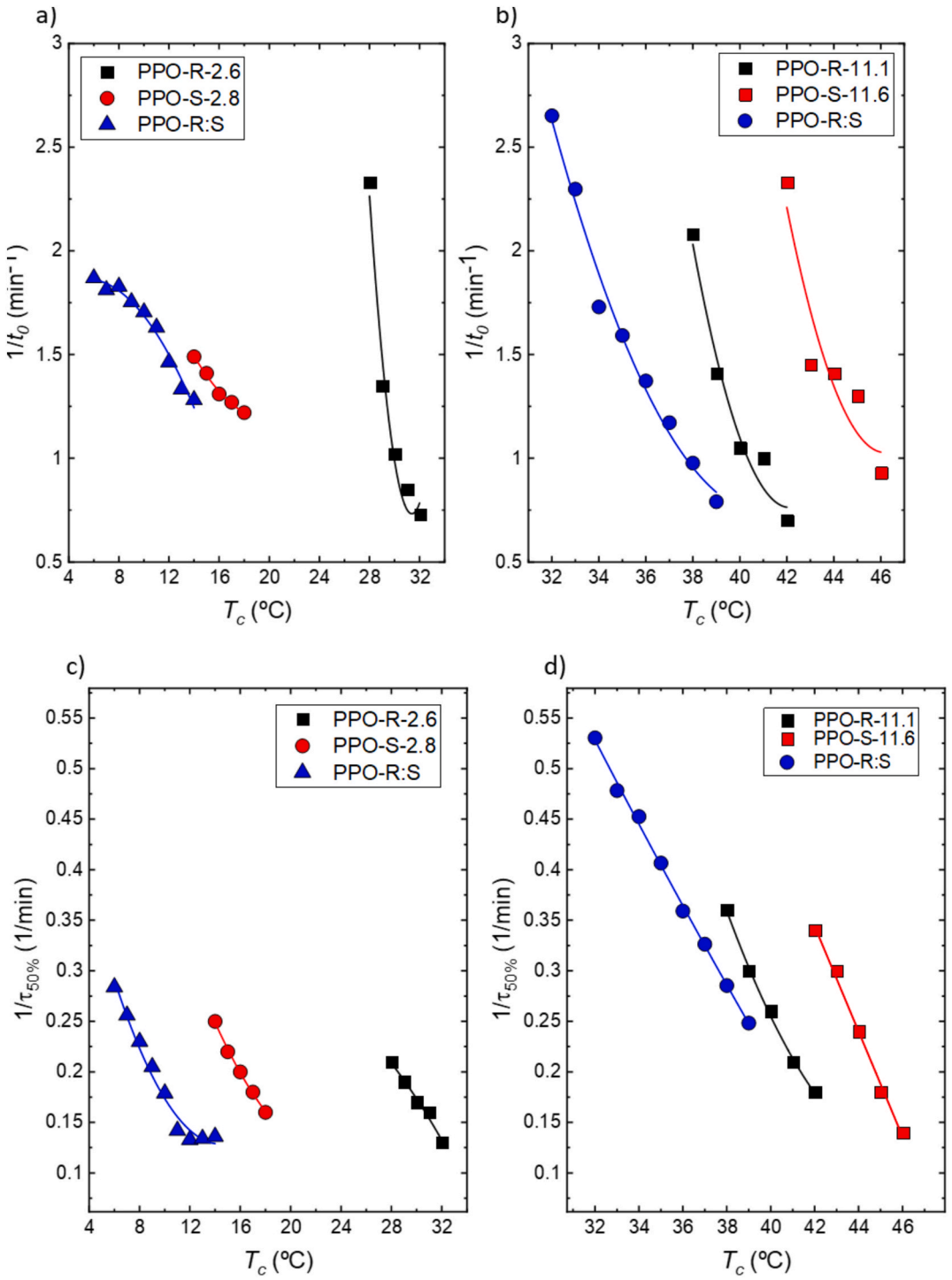

Fig. 12. Inverse of induction time ($1/t_0$) as a function of T_c for a) low M_n and b) high M_n PPO samples. Inverse of half-crystallization time ($1/\tau_{50\%}$) as a function of T_c for c) low M_n and d) high M_n PPO samples.

approaching a plateau at high M_n regardless of stereoconfiguration. Morphologically, both enantiomers displayed negative, banded spherulites whose periodicity depended on crystallization temperature. Structurally, WAXS and SAXS confirmed that all samples crystallize into identical orthorhombic unit cells and lamellar architectures, independent of M_n or stereoconfiguration.

A stereoconfiguration-dependent trend was identified across multiple measurements. At low M_n, PPO-*R* displayed higher thermal transitions and faster crystallization kinetics than PPO-*S*, whereas at high M_n, this trend reversed, with PPO-*S* becoming the faster crystallizing species. Although such an M_n-dependent inversion is unexpected for two enantiomeric polymers that crystallize into identical lattices, its consistent appearance across nucleation, growth, overall crystallization rate, and non-isothermal transitions confirms that the effect is real and reproducible experimentally. We have explained these results with the tentative hypothesis that stereoconfiguration may subtly influence melt-state mobility rather than crystalline structure. This needs further confirmation by rheology and spectroscopic techniques.

The distinct banding periodicities observed for PPO-*R* and PPO-*S* also support the possibility that the preferred helicoidal conformations

adopted in the melt are not perfectly equivalent, which may lead to small differences in segmental mobility and in the onset of entanglement-controlled dynamics. These dynamic considerations offer a tentative but coherent explanation for the molecular-weight-dependent inversion in crystallization kinetics. SSA experiments further showed that these stereoconfiguration-dependent differences persist even under near-equilibrium fractionation conditions, reinforcing the view that their origin may reside in melt dynamics rather than in solid-state structural variations.

In the second part of the study, racemic PPO-*R*:*S* blends were investigated. These blends did not form stereocomplexes but exhibited systematically reduced thermal transitions, nucleation rates, spherulitic growth rates, and overall crystallization rates compared to the pure enantiomeric PPOs. This kinetic retardation is consistent with a possible packing frustration between chains of opposite helical senses, which could disrupt the conformational coherence required for efficient lamellar assembly. The effect is independent of M_n and provides a practical strategy for tuning crystallization kinetics in PPO-based materials. Blending the two enantiomers, or adjusting their M_n, enables deliberate slowing of crystallization, an advantageous feature for processing and for tailoring blends or copolymers with biodegradable polyesters such as PLA. These insights underscore the potential of PPO to tune crystallization behavior, broaden processing windows, and enable novel applications in packaging and biomedical materials.

5. Supporting Information

Methodological details, NMR, SEM, DSC cooling at various cooling rates and subsequent heatings at constant heating rate and during isothermal measurement, WAXS/SAXS patterns taken, in real-time, during cooling and heating ramps and PLOM taken during cooling and heating ramps and isothermal process. Comparisons of relevant parameters as a function of M_n by SEC and NMR. Details regarding the application of the Avrami and Lauritzen and Hoffman theories.

CRediT authorship contribution statement

Juan Torres-Rodríguez: Writing – original draft, Validation, Methodology, Investigation, Formal analysis, Data curation. **Charlotte Fornaciari:** Writing – review & editing, Methodology, Investigation, Formal analysis, Data curation, Conceptualization. **Ricardo A. Pérez-Camargo:** Writing – review & editing, Visualization, Validation, Methodology, Conceptualization. **Agurtzane Mugica:** Writing – review & editing, Visualization. **Manuela Zubitur:** Writing – review & editing, Visualization. **Giovanni Preda:** Writing – review & editing, Supervision. **Dario Pasini:** Writing – review & editing, Supervision. **Olivier Coulembier:** Writing – review & editing, Visualization, Supervision, Project administration, Conceptualization. **Alejandro J. Müller:** Writing – review & editing, Visualization, Supervision, Project administration, Conceptualization.

Declaration of competing interest

The authors declare that they have no known competing financial interests or personal relationships that could have appeared to influence the work reported in this paper.

Acknowledgements

The authors thank Istituto Nazionale Previdenza Sociale (INPS, Italy) for a Ph.D. fellowship to C.F., the University of Pavia, and MIUR (D.P.) for funding. O.C. is a Senior Research Associate for the F.R.S.-FNRS of Belgium and AXA Professor in Chemistry. This work has received funding from the Department of Education of the Basque Government through grant no. IT1503-22, and from the María de Maeztu Excellence Unit CEX2023-001303-M funded by MCIN/AEI/10.13039/501100011033. R.A.P – C is supported by the ADAGIO-H2020-MSCA COFUND-2020 program (101034379). The authors performed synchrotron radiation WAXS/SAXS experiments at BL11-NCD-SWEET beamline at the ALBA Synchrotron (Proposal Number 2022086944). We also acknowledge the collaboration of the ALBA Synchrotron radiation facilities staff.

Appendix A. Supplementary material

Supplementary data to this article can be found online at https://doi.org/10.1016/j.eurpolymj.2025.114464.

Data availability

Data will be made available on request.

References

[1] M.S. Ganewatta, Z. Wang, C. Tang, Chemical syntheses of bioinspired and biomimetic polymers toward biobased materials, Nat. Rev. Chem. 5 (2021) 753–772, https://doi.org/10.1038/s41570-021-00325-x.
[2] J.G. Rosenboom, R. Langer, G. Traverso, Bioplastics for a circular economy, Nat. Rev. Mater. 7 (2022) 117–137, https://doi.org/10.1038/s41578-021-00407-8.
[3] T. Beslikas, I. Gigis, V. Goulios, J. Christoforides, G.Z. Papageorgiou, D.N. Bikiaris, Crystallization study and comparative in vitro-in vivo hydrolysis of PLA reinforcement ligament, Int. J. Mol. Sci. 12 (2011) 6597–6618, https://doi.org/10.3390/ijms12106597.
[4] T.A.P. Engels, S.H.M. Söntjens, T.H. Smit, L.E. Govaert, Time-dependent failure of amorphous polylactides in static loading conditions, J. Mater. Sci. Mater. Med. 21 (2010) 89–97, https://doi.org/10.1007/s10856-009-3851-9.
[5] G. Gorrasi, R. Pantani, Effect of PLA grades and morphologies on hydrolytic degradation at composting temperature: Assessment of structural modification and kinetic parameters, Polym. Degrad. Stab. 98 (2013) 1006–1014, https://doi.org/10.1016/j.polymdegradstab.2013.02.005.
[6] M. Hakkarainen, A.-C. Albertsson, Degradation Products of Aliphatic and Aliphatic–Aromatic Polyesters, in: A.-.-C. Albertsson, M. Hakkarainen (Eds.), Chromatography for Sustainable Polymeric Materials: Renewable, Degradable and Recyclable, Springer Berlin Heidelberg, Berlin, Heidelberg, 2008, pp. 85–116, https://doi.org/10.1007/12_2007_128.
[7] S. Li, H. Garreau, M. Vert, Structure-property relationships in the case of the degradation of massive poly(α-hydroxy acids) in aqueous media, J. Mater. Sci. Mater. Med. 1 (1990) 198–206, https://doi.org/10.1007/BF00701077.
[8] H. Antheunis, J.-C. van der Meer, M. de Geus, W. Kingma, C.E. Koning, Improved mathematical model for the hydrolytic degradation of aliphatic polyesters, Macromolecules 42 (2009) 2462–2471, https://doi.org/10.1021/ma802222m.
[9] Q. Liu, C. Cai, C.-M. Dong, Poly(L-lactide)-b-poly(ethylene oxide) copolymers with different arms: hydrophilicity, biodegradable nanoparticles, in vitro degradation, and drug-release behavior, J. Biomed. Mater. Res. A 88A (2009) 990–999, https://doi.org/10.1002/jbm.a.31945.
[10] S.K. Agrawal, N. Sanabria-DeLong, G.N. Tew, S.R. Bhatia, Structural characterization of PLA−PEO−PLA solutions and hydrogels: crystalline vs amorphous PLA domains, Macromolecules 41 (2008) 1774–1784, https://doi.org/10.1021/ma070634r.
[11] L.M.D. Loiola, M.A. de Farias, R.V. Portugal, M.I. Felisberti, Amphiphilic polylactide-poly(ethylene oxide)-poly(propylene oxide) block copolymers: self-assembly behavior and cell affinity, J. Polym. Sci. A Polym. Chem. 56 (2018) 2203–2213, https://doi.org/10.1002/pola.29189.
[12] C. Chen, L. Chen, L. Cao, W. Shen, L. Yu, J. Ding, Effects of l-lactide and d,l-lactide in poly(lactide-co-glycolide)-poly(ethylene glycol)-poly(lactide-co-glycolide) on the bulk states of triblock copolymers, and their thermogellation and biodegradation in water, RSC Adv. 4 (2014) 8789–8798, https://doi.org/10.1039/C3RA47494A.
[13] T. Iwata, Y. Doi, Morphology and enzymatic degradation of poly(l-lactic acid) single crystals, Macromolecules 31 (1998) 2461–2467, https://doi.org/10.1021/ma980008h.
[14] L. Yang, X. Qi, P. Liu, A. El Ghzaoui, S. Li, Aggregation behavior of self-assembling polylactide/poly(ethylene glycol) micelles for sustained drug delivery, Int. J. Pharm. 394 (2010) 43–49, https://doi.org/10.1016/j.ijpharm.2010.04.030.
[15] Y. Hu, Y.S. Hu, V. Topolkaraev, A. Hiltner, E. Baer, Aging of poly(lactide)/poly (ethylene glycol) blends. part 2. poly(lactide) with high stereoregularity, Polymer (Guildf) 44 (2003) 5711–5720, https://doi.org/10.1016/S0032-3861(03)00615-3.
[16] Y. Hu, M. Rogunova, V. Topolkaraev, A. Hiltner, E. Baer, Aging of poly(lactide)/poly(ethylene glycol) blends. part 1. poly(lactide) with low stereoregularity, Polymer (Guildf) 44 (2003) 5701–5710, https://doi.org/10.1016/S0032-3861(03)00614-1.
[17] L. Gu, E.E. Nessim, T. Li, C.W. Macosko, Toughening poly(lactic acid) with poly (ethylene oxide)-poly(propylene oxide)-poly(ethylene oxide) triblock copolymers, Polymer (Guildf) 156 (2018) 261–269, https://doi.org/10.1016/j.polymer.2018.09.027.

[18] C.C. Price, M. Osgan, R.E. Hughes, C. Shambelan, The polymerization of L-propylene oxide, J. Am. Chem. Soc. 78 (1956) 690–691, https://doi.org/10.1021/ja01584a049.
[19] F. García, R. Gómez, L. Sánchez, Chiral supramolecular polymers, Chem. Soc. Rev. 52 (2023) 7524–7548, https://doi.org/10.1039/d3cs00470h.
[20] M. Srinivasarao, Chirality and polymers, Curr. Opin. Colloid Interface Sci. 4 (1999) 147–152, https://doi.org/10.1016/S1359-0294(99)00024-2.
[21] E. Stanley, M. Litt, Crystal structure of d,L poly (propylene oxide), J. Polym. Sci. 43 (1960) 453–458, https://doi.org/10.1002/pol.1960.1204314215.
[22] J.H. Magill, Crystallization and Morphology of d, Z-and bPoly(Propy1ene Oxide), Macromol. Chem. 86 (1965) 283–288, https://doi.org/10.1002/macp.1965.020860125.
[23] M.H. Hutchinson, J.R. Dorgan, D.M. Knauss, S.B. Hait, Optical properties of polylactides, J. Polym. Environ. 14 (2006) 119–124, https://doi.org/10.1007/s10924-006-0001-z.
[24] M.I. Childers, A.K. Vitek, L.S. Morris, P.C.B. Widger, S.M. Ahmed, P. M. Zimmerman, G.W. Coates, Isospecific, chain shuttling polymerization of propylene oxide using a bimetallic chromium catalyst: a new route to semicrystalline polyols, J. Am. Chem. Soc. 139 (2017) 11048–11054, https://doi.org/10.1021/jacs.7b00194.
[25] F.M. De Souza, P.K. Kahol, R.K. Gupta, Introduction to polyurethane chemistry, in: Polyurethane chemistry: Renewable polyols and isocyanates, American Chemical Society, 2021, pp. 1–24, https://doi.org/10.1021/bk-2021-1380.ch001.
[26] C. Booth, C.J. Devoy, G. Gee, Heat of fusion of isotactic poly(propylene oxide), Polymer (Guildf) 12 (1971) 327–334, https://doi.org/10.1016/0032-3861(71)90055-3.
[27] W. Cooper, D.E. Eaves, G. Vaughan, Melting characteristics of isotactic polypropylene oxide, Polymer (Guildf) 8 (1967) 273–280, https://doi.org/10.1016/0032-3861(67)90030-4.
[28] L.G.M. Beekmans, M.A. Hempenius, G.J. Vancso, Morphological development of melt crystallized poly(propylene oxide) by in situ AFM: formation of banded spherulites, Eur. Polym. J. 40 (2004) 893–903, https://doi.org/10.1016/j.eurpolymj.2004.01.025.
[29] M.A. Kennedy, G.R. Brown, L.E. St-pierre, Crystallization of isotactic (D,L) poly (propylene oxide) in the presence of fine-particle silica. I: Radial growth rates of spherulites, Polym. Eng. Sci. 30 (1990) 769–775, https://doi.org/10.1002/pen.760301304.
[30] N. López-Rodríguez, I. Martínez de Arenaza, E. Meaurio, J.R. Sarasua, Improvement of toughness by stereocomplex crystal formation in optically pure polylactides of high molecular weight, J. Mech. Behav. Biomed. Mater. 37 (2014) 219–225, https://doi.org/10.1016/j.jmbbm.2014.05.022.
[31] J.R. Sarasua, A.L. Arraiza, P. Balerdi, I. Maiza, Crystallization and thermal behaviour of optically pure polylactides and their blends, J. Mater. Sci. 40 (2005) 1855–1862, https://doi.org/10.1007/s10853-005-1204-8.
[32] H. Tsuji, K. Tashiro, L. Bouapao, M. Hanesaka, Synchronous and separate homo-crystallization of enantiomeric poly(l-lactic acid)/poly(d-lactic acid) blends, Polymer (Guildf) 53 (2012) 747–754, https://doi.org/10.1016/j.polymer.2011.12.023.
[33] J. Zhang, Y. Duan, H. Sato, H. Tsuji, I. Noda, S. Yan, Y. Ozaki, Crystal modifications and thermal behavior of poly(l-lactic acid) revealed by infrared spectroscopy, Macromolecules 38 (2005) 8012–8021, https://doi.org/10.1021/ma051232r.
[34] S. Saeidlou, M.A. Huneault, H. Li, C.B. Park, Poly(lactic acid) crystallization, Prog. Polym. Sci. 37 (2012) 1657–1677, https://doi.org/10.1016/j.progpolymsci.2012.07.005.
[35] J.R. Dorgan, J. Janzen, M.P. Clayton, S.B. Hait, D.M. Knauss, Melt rheology of variable L-content poly(lactic acid), J. Rheol. (N Y N Y) 49 (2005) 607–619, https://doi.org/10.1122/1.1896957.
[36] R.M. Michell, V. Ladelta, E. Da Silva, A.J. Müller, N. Hadjichristidis, Poly(lactic acid) stereocomplexes based molecular architectures: synthesis and crystallization, Prog. Polym. Sci. 146 (2023) 101742, https://doi.org/10.1016/j.progpolymsci.2023.101742.
[37] M.L. Di Lorenzo, M. Raimo, E. Cascone, E. Martuscelli, Poly (3-hydroxybutyrate)-based copolymers and blends: influence of a second component on crystallization and thermal behavior, J. Macromol. Sci. B 40 (2001) 639–667, https://doi.org/10.1081/MB-100107554.
[38] J. Bruckmoser, S. Pongratz, L. Stieglitz, B. Rieger, Highly isoselective ring-opening polymerization of rac-β-butyrolactone: access to synthetic poly(3-hydroxybutyrate) with polyolefin-like material properties, J. Am. Chem. Soc. 145 (2023) 11494–11498, https://doi.org/10.1021/jacs.3c02348.
[39] M. Guo, W. Wu, W. Wu, R. Wang, L. Huang, Q. Gao, Recent advances in enhancing stereocomplexation between poly(lactide) enantiomeric chains, Phys. Chem. Chem. Phys. 25 (2023) 17737–17758, https://doi.org/10.1039/D3CP01003A.
[40] F. Luo, A. Fortenberry, J. Ren, Z. Qiang, Recent progress in enhancing poly(lactic acid) stereocomplex formation for material property improvement, Front. Chem. 8 (2020), https://doi.org/10.3389/fchem.2020.00688.
[41] H.S. Park, C.K. Hong, Relationship between the stereocomplex crystallization behavior and mechanical properties of plla/pdla blends, Polymers (Basel) 13 (2021), https://doi.org/10.3390/polym13111851.
[42] M.R. Caputo, C. Shi, X. Tang, H. Sardon, E.-Y.-X. Chen, A.J. Müller, Tailoring the nucleation and crystallization rate of polyhydroxybutyrate by copolymerization, Biomacromolecules 24 (2023) 5328–5341, https://doi.org/10.1021/acs.biomac.3c00808.
[43] R.A. Pérez-Camargo, G.M. Liu, D.J. Wang, A.J. Müller, Experimental and data fitting guidelines for the determination of polymer crystallization kinetics, Chin. J. Polym. Sci. 40 (2022) 658–691, https://doi.org/10.1007/s10118-022-2724-2.
[44] A.T. Lorenzo, M.L. Arnal, J. Albuerne, A.J. Müller, DSC isothermal polymer crystallization kinetics measurements and the use of the Avrami equation to fit the data: guidelines to avoid common problems, Polym. Test. 26 (2007) 222–231, https://doi.org/10.1016/j.polymertesting.2006.10.005.
[45] A.J. Muller, Z.H. Hernandez, M.L. Arnal, J.J. Sanchez, Successive self-nucleation/annealing (SSA): a novel technique to study molecular segregation during crystallization, Polym. Bull. 39 (1997) 465–472, https://doi.org/10.1007/s002890050174.
[46] A.J. Müller, M.L. Arnal, Thermal fractionation of polymers, Prog. Polym. Sci. 30 (2005) 559–603, https://doi.org/10.1016/j.progpolymsci.2005.03.001.
[47] A.J. Müller, R.M. Michell, R.A. Pérez, A.T. Lorenzo, Successive self-nucleation and annealing (ssa): correct design of thermal protocol and applications, Eur. Polym. J. 65 (2015) 132–154, https://doi.org/10.1016/j.eurpolymj.2015.01.015.
[48] R.A. Pérez-Camargo, D. Cavallo, A.J. Müller, Recent applications of the successive self-nucleation and annealing thermal fractionation technique, Front. Soft Matter 2 (2022), https://doi.org/10.3389/frsfm.2022.1003500.
[49] B. Fillon, J.C. Wittmann, B. Lotz, A. Thierry, Self-nucleation and recrystallization of isotactic polypropylene (α phase) investigated by differential scanning calorimetry, J. Polym. Sci. B Polym. Phys. 31 (1993) 1383–1393, https://doi.org/10.1002/polb.1993.090311013.
[50] A.J. Müller, V. Balsamo, M.L. Arnal, T. Jakob, H. Schmalz, V. Abetz, Homogeneous nucleation and fractionated crystallization in block copolymers, Macromolecules 35 (2002) 3048–3058, https://doi.org/10.1021/ma012026w.
[51] L. Sangroniz, D. Cavallo, A.J. Müller, Self-nucleation effects on polymer crystallization, Macromolecules 53 (2020) 4581–4604, https://doi.org/10.1021/acs.macromol.0c00223.
[52] R.M. Michell, A. Mugica, M. Zubitur, A.J. Müller, Self-nucleation of crystalline phases within homopolymers, polymer blends, copolymers, and nanocomposites, Polymer crystallization I: From chain microstructure to processing (2015) 215–256, https://doi.org/10.1007/12_2015_327.
[53] C. Fornaciari, D. Pasini, O. Coulembier, Controlled oxyanionic polymerization of propylene oxide: unlocking the molecular-weight limitation by a soft nucleophilic catalysis, Macromol. Rapid Commun. 43 (2022), https://doi.org/10.1002/marc.202200424.
[54] G. Giacomelli, L. Lardicci, R. Menicagli, L. Bertero, Chiral discrimination in the isomerization of racemic 1-olefins by an optically active organoaluminium–nickel system, J. Chem. Soc. Chem. Commun. (1979) 633–634, https://doi.org/10.1039/C39790000633.
[55] E.H. Sharman, O. Schnepp, P. Salvadori, C. Bertucci, L. Lardicci, Circular dichroism spectra of aliphatic ethers, J. Chem. Soc. Chem. Commun. 22 (1979) 1000–1001, https://doi.org/10.1039/C39790001000.
[56] B. Crist, J.M. Schultz, Polymer spherulites: a critical review, Prog. Polym. Sci. 56 (2016) 1–63, https://doi.org/10.1016/j.progpolymsci.2015.11.006.
[57] E. Yashima, K. Maeda, H. Iida, Y. Furusho, K. Nagai, Helical polymers: synthesis, structures, and functions, Chem. Rev. 109 (2009) 6102–6211, https://doi.org/10.1021/cr900162q.
[58] Y. Okamoto, Precision synthesis, structure and function of helical polymers, Proc. Jpn. Acad. Ser. B Phys. Biol. Sci. 91 (2015) 246–261, https://doi.org/10.2183/pjab.91.246.
[59] H.-M. Ye, J.-S. Wang, S. Tang, J. Xu, X.-Q. Feng, B.-H. Guo, X.-M. Xie, J.-J. Zhou, L. Li, Q. Wu, G.-Q. Chen, Surface stress effects on the bending direction and twisting chirality of lamellar crystals of chiral polymer, Macromolecules 43 (2010) 5762–5770, https://doi.org/10.1021/ma100920u.
[60] M.-C. Li, H.-F. Wang, C.-H. Chiang, Y.-D. Lee, R.-M. Ho, Lamellar-twisting-induced circular dichroism of chromophore moieties in banded spherulites with evolution of homochirality, Angew. Chem. Int. Ed. 53 (2014) 4450–4455, https://doi.org/10.1002/anie.201310078.
[61] B. Lotz, S.Z.D. Cheng, A critical assessment of unbalanced surface stresses as the mechanical origin of twisting and scrolling of polymer crystals, Polymer (Guildf) 46 (2005) 577–610, https://doi.org/10.1016/j.polymer.2004.07.042.
[62] J. Xu, H. Ye, S. Zhang, B. Guo, Organization of twisting lamellar crystals in birefringent banded polymer spherulites: a mini-review, Crystals (Basel) 7 (2017), https://doi.org/10.3390/cryst7080241.
[63] J.D. Hoffman, J.I. Lauritzen, Crystallization of bulk polymers with chain folding: theory of growth of lamellar spherulites, J. Res. Natl. Bur. Stand. Phys. Chem. 65 (1961) 197–336, https://doi.org/10.6028/jres.065A.035.
[64] D. Cavallo, A.J. Müller, Polymer crystallization, macromolecular, Engineering (2022) 1–57, https://doi.org/10.1002/9783527815562.mme0032.
[65] U.W. Gedde, M.S. Hedenqvist, Fundamental polymer science, Vol. 2, Springer, Cham, 2019, https://doi.org/10.1007/978-3-030-29794-7.
[66] B. Hsiao, Polymer crystallization: the development of crystalline order in thermoplastic polymers, J. Am. Chem. Soc. 124 (2002) 7251–7252, https://doi.org/10.1021/ja015359h.
[67] R.M. Michell, A.J. Müller, Confined crystallization of polymeric materials, Prog. Polym. Sci. 54–55 (2016) 183–213, https://doi.org/10.1016/j.progpolymsci.2015.10.007.
[68] N. Okui, S. Umemoto, R. Kawano, A. Mamun, Temperature and Molecular Weight Dependencies of Polymer Crystallization, in: G. Reiter, G.R. Strobl (Eds.), Progress in Understanding of Polymer Crystallization, Springer Berlin Heidelberg, Berlin, Heidelberg, 2007, pp. 391–425, https://doi.org/10.1007/3-540-47307-6_19.
[69] L. Mandelkern. Crystallization of polymers: volume 2, kinetics and mechanisms, Cambridge University Press, 2004, https://doi.org/10.1017/CBO9780511535413.
[70] A. Fernández-Tena, R.A. Pérez-Camargo, O. Coulembier, L. Sangroniz, N. Aranburu, G. Guerrica-Echevarria, G. Liu, D. Wang, D. Cavallo, A.J. Müller, Effect of molecular weight on the crystallization and melt memory of poly

(ϵ-caprolactone) (PCL), Macromolecules 56 (2023) 4602–4620, https://doi.org/10.1021/acs.macromol.3c00234.
[71] G. Allen, C. Booth, M.N. Jones, D.J. Marks, W.D. Taylor, Polypropylene oxide iii—crystallizability, fusion and glass formation, Polymer (guildf) 5 (1964) 547–552, https://doi.org/10.1016/0032-3861(64)90205-8.
[72] J.D. Menczel, L. Judovits, R.B. Prime, H.E. Bair, M. Reading, S. Swier, Differential scanning calorimetry (DSC), Thermal analysis of polymers: Fundamentals and applications (2009) 7–239, https://doi.org/10.1002/9780470423837.ch2.
[73] M.R. Caputo, X. Tang, A.H. Westlie, H. Sardon, E.Y.X. Chen, A.J. Müller, Effect of chain stereoconfiguration on poly(3-hydroxybutyrate) crystallization kinetics, Biomacromolecules 23 (2022) 3847–3859, https://doi.org/10.1021/acs.biomac.2c00682.
[74] L. Sangroniz, L. Meabe, A. Basterretxea, H. Sardon, A.J. Müller, D. Cavallo, Chemical structure drives memory effects in the crystallization of homopolymers, Macromolecules 53 (2020) 4874–4881, https://doi.org/10.1021/acs.macromol.0c00751.
[75] R.A. Pérez, M.E. Córdova, J.V. López, J.N. Hoskins, B. Zhang, S.M. Grayson, A. J. Müller, Nucleation, crystallization, self-nucleation and thermal fractionation of cyclic and linear poly(ε-caprolactone)s, React. Funct. Polym. 80 (2014) 71–82, https://doi.org/10.1016/j.reactfunctpolym.2013.10.013.
[76] M. Avrami, Kinetics of phase change. ii transformation-time relations for random distribution of nuclei, J. Chem. Phys. 8 (1940) 212–224, https://doi.org/10.1063/1.1750631.
[77] M. Avrami, Granulation, phase change, and microstructure kinetics of phase change. III, J. Chem. Phys. 9 (1941) 177–184, https://doi.org/10.1063/1.1750872.
[78] B. Wu, C.J. Harlan, R.W. Lenz, A.R. Barron, Stereoregular polymerization of (R,S)-propylene oxide by an alumoxane−propylene oxide complex, Macromolecules 30 (1997) 316–318, https://doi.org/10.1021/ma9601934.